Spatiotemporally resolved heat transfer measurements in falling liquid-films by simultaneous application of planar laser-induced fluorescence (PLIF), particle tracking velocimetry (PTV) and infrared (IR) thermography

Alexandros Charogiannis[1,2] and Christos N. Markides[*1]

[1]*Clean Energy Processes (CEP) Laboratory, Department of Chemical Engineering, Imperial College London, London SW7 2AZ, United Kingdom*
[2]*LaVision UK Ltd, United Kingdom*

December 4, 2018

Abstract

We present an optical technique that combines simultaneous planar laser-induced fluorescence (PLIF), particle tracking velocimetry (PTV) and infrared (IR) thermography for the space-and time-resolved measurement of the film-height, 2-D velocity and 2-D free-surface temperature in liquid films falling over an inclined, resistively-heated glass substrate. Using this information and knowledge of the wall temperature, local and instantaneous heat-transfer coefficients (HTCs) and Nusselt numbers, Nu, are also recovered along the waves of liquid films with Kapitza number, $Ka = 180$, and Prandtl number, $Pr = 77$. By employing this technique, falling-film flows are investigated with Reynolds numbers in the range $Re = 18 - 66$, wave frequencies set to $f_w = 7$, 12 and 17 Hz, and a wall heat flux set to $\dot{q} = 2.5$ W cm^{-2}. Complementary data are also collected in equivalent (i.e., for the same mean-flow Re) flows with $\dot{q} = 0$ W cm^{-2}. Quality assurance experiments are performed that reveal deviations of up to 2-3% between PLIF/PTV-derived film heights, interfacial/bulk velocities and flow rates, and both analytical predictions and direct measurements of flat films over a range of conditions, while IR-based temperature measurements fall within 1 °C of thermocouple measurements. Highly localized film height, velocity, flow-rate and interface-temperature data are generated along the examined wave topologies by phase/wave locked averaging. The application of a heat flux ($\dot{q} = 2.5$ W cm^{-2}) results in a pronounced "thinning" of the investigated films (by 18%, on average), while the mean bulk velocities compensate by increasing by a similar extent to conserve the imposed flow rate. The axial-velocity profiles that are obtained in the heated cases are parabolic but "fuller" compared to equivalent isothermal flows, excluding any wave-regions where the interface slopes are high. As the Re is reduced, the heating applied at the wall penetrates through the film, resulting in a pronounced coupling between the HTC and the film height in thinner film regions. When the imposed wave frequency is increased, a narrower range of HTCs is observed, which we link to the evolution of the film topology and the associated redistribution of the fluid flow upstream of the imaging location, as the liquid viscosity decreases. The local and instantaneous Nu is strongly coupled to the film height and experiences variations that increase as f_w is reduced.

1 Introduction

1.1 Background and motivation

The hydrodynamics of wavy, falling liquid-films are strongly dependent on the imposition of heating on the substrate side [1, 2], the presence and direction of a gas-shear flow [3, 4], and the direction of gravity which may act to stabilise or destabilise the flow [5, 6]. Some of these flow configurations are encountered in engineering and industrial equipment, while others act as model systems that allow physical phenomena of interest, such as the formation, amplification and saturation of hydrodynamic waves on the film free-surface, to be studied in detail. The widespread employment of falling liquid-films in the solar, nuclear, oil and gas and process engineering industries where they play a prominent role in the design of improved, compact and cost-effective means of heat and mass transfer, along with the strong scientific interest in the flow phenomena that govern these flows, have motivated numerous academic studies that have yielded hundreds of research articles. In the field of experimental fluid mechanics, the advent of laser diagnostics since the late 1980s facilitated a number of fascinating studies of the complex flow phenomena underlying falling-film flows, thus promoting the development of advanced numerical tools. Ongoing experimental efforts seek to overcome some of the fundamental challenges associated with *in situ*, time-and space resolved flow and heat transfer

measurements in these flows, such as the sub-mm domains under observation and the moving and wavy interface which causes significant optical distortions. In addition, they are often aimed at the study of more complex systems and the simultaneous measurement of multiple flow parameters.

In this paper we build upon our previous, combined experimental/numerical study of the hydrodynamic characteristics of isothermal falling films as a function of the liquid Kapitza number, Ka, the flow Reynolds number, Re, and the wave frequency, f_w (see Refs. [7–11]), the experimental investigation of spatiotemporally resolved heat transfer in low Prandtl number, Pr (= 5.4), water-ethanol flows (see Refs. [12, 13]), and the experimental investigation of the topology of liquid films falling under an inclined planar-substrate [6, 14]. Specifically, we investigate the unsteady heat transfer in harmonically excited liquid-films falling over an inclined, electrically-heated glass substrate by pursuing simultaneous, space- and time-resolved film-height, 2-D velocity and 2-D free-surface (gas-liquid interface) temperature measurements. These are recovered by simultaneous application of planar laser-induced fluorescence (PLIF), particle tracking velocimetry (PTV) and infrared (IR) thermography, respectively. Based on this data and knowledge of the applied heat-flux and the substrate (solid-liquid interface) temperature at the PLIF/PTV imaging location, local and instantaneous heat-transfer coefficient (HTC) and Nusselt number, Nu data are also generated. Before proceeding with a discussion of select, relevant research articles, we would like to emphasize that to the best of our knowledge, this is the first instance whereby spatiotemporally resolved heat-transfer measurements are reported simultaneously with spatiotemporally resolved flow measurements in falling liquid-films.

1.2 Measurement techniques

A broad range of measurement techniques have been developed or adapted from other applications towards the detailed study of falling film-flows in response to the strong and continuing interest by the industry and scientific community. Optical diagnostics allow for real-time, *in situ* imaging of one- (1-D), two- (2-D) or three-dimensional (3-D) spatial distributions of seeded or naturally occurring tracer-molecules or particles, and are therefore often preferred to more "conventional" approaches, including instrumentation such as thermocouples, and conductivity and capacitance probe measurements. Fluorescence-based techniques, in particular, have been employed in a wide range of multiphase flows for the identification of interfaces [15, 16], the investigation of gas and liquid entrainment [17, 18], the identification of mixing zones [19–22], and the measurement of temperature [13, 23] and velocity [24, 25]. Planar laser-induced fluorescence (PLIF), which we currently employ in order to recover the film-height, relies on the (planar) illumination of a section of the flow, and the subsequent collection of the fluorescence emitted by the dye-seeded liquid over the excitation plane. Thus, a significant advantage of this approach is that the fluid domain is visualised directly; a feature that can be fully exploited when PLIF is combined with other optical techniques such as particle image/tracking velocimetry (PIV/PTV). Examples of the application of PLIF in isothermal film flows can be found in our

previous work, as well as in Refs. [16, 26, 27].

An important attribute of fluorescence-based techniques is that the emission characteristics of common fluorescent markers often depend on flow parameters such as the temperature and pressure, as well as on the concentration of other species that may be present in the flow and that can sensitize or quench the emission, such as oxygen. Regarding heated film-flow investigations, the temperature-sensitivity of the emitted fluorescence may or may not be desirable; when it is, it can be exploited to yield temperature measurements. For example, Markides *et al.* [12, 13] combined PLIF-based film-height and temperature measurements (at the gas-liquid interface) with IR-based temperature measurements (at the solid-liquid interface) in laminar and transitional falling-film flows over a heated titanium-foil. Depending on the film topology and the flow Re, the authors reported significant heat transfer enhancements compared to predictions from the steady-flow analysis, which they attributed to convective gains and the development of Marangoni flows (thermal rivulets) on the free surface.

In contrast to these studies where a single fluorescent marker was employed, PLIF-based temperature measurements can also be made using the ratio of the fluorescence emitted by two dyes with different temperature sensitivities (see, for example, Refs. [28, 29]). Depending on the selected dyes, such "ratiometric" techniques can achieve significantly higher temperature sensitivity (up to 7% °C^{-1}), as well as improved accuracy, as some fluorescence-emission dependencies such as the excitation energy cancel out in the image ratio. Furthermore, this approach can be used to generate temperature field (i.e., 2-D) measurements (see, for example, Refs. [30, 31] where the performance of various microfluidic devices was examined in detail). A significant limitation of the ratiometric approach is the increased experimental complexity, as two cameras and possibly two excitation wavelengths may be required. As an alternative to fluorescence imaging, researchers from RWTH Aachen exploited the different temperature dependencies of the fluorescence and phosphorescence emission of diacetyl in order to conduct simultaneous film-height and temperature measurements [23, 32]. In line with the results of Markides *et al.*, the authors observed a strong correlation between the film height and the HTC, and reported significant enhancements ($\approx$ 80%) at the wave troughs of a laminar water-film with $Re = 126$.

As an alternative to PLIF, the fluorescence emitted by the illuminated liquid volume has also been used to quantify the film-height (see, for example, Refs,[33–35]). This technique, which is typically referred to as brightness-based laser-induced fluorescence (BBLIF), must be calibrated *in situ*, and requires corrections for the spatial inhomogeneity, pulse-to-pulse variation and reduction of the excitation energy along the path of the laser sheet in order to yield accurate results. Moreover, it does not allow for direct flow-field visualisation, but can be used to generate film height measurements over an extended fluid domain. In a recent publication, BBLIF was employed simultaneously with PLIF in annular gas-liquid flows, and was shown to offer an accurate measurement of film thickness when the interface is smooth, the film is relatively thin and any interface gradients are small [36]. In contrast, when the film surface is "rougher"

and/or when there is extensive gas/liquid entrainment in the liquid/gas phases, the accuracy of this technique is compromised. Nevertheless, it should be noted that refraction of the emitted fluorescence at the gas-liquid interface and the presence of bubbles ahead of and behind the excited film region still hamper the identification of the true interface in the case of PLIF.

Referring to heated film-flow investigations, BBLIF has been used extensively researchers from the Kutateladze Institute of Thermophysics of the Siberian Branch of the Russian Academy of Sciences, and specifically their investigations of the formation of rivulets due to thermocapillary (Marangoni) convection and the associated heat transfer gains. Chinnov and Kabov [37], for example, reported that the distance between adjacent rivulets depends weakly on the film inclination angle above 15 °, and that the rivulet amplitude increases with increasing distance from the inlet due to the temperature gradient in the streamwise direction of the flow. The dependence of the rivulet wavelength on the flow Re and the applied heat flux were examined in greater detail in Refs. [38, 39], where shorter wavelengths were observed at higher heat fluxes, as well as at higher Re. It should be noted that any temperature dependence of the fluorescence intensity was suppressed by employment of Rhodamnine 6G, a fluorescent marker that displays only limited sensitivity to temperature.

Along with LIF, IR was employed in the aforementioned studies in order to link the observed interfacial temperature-distributions with the Marangoni-driven interface deformations. These measurements rely on the high emissivity of common liquids in the mid-wave infared (MWIR), including water and glycerol, which render them effectively opaque when the emitted IR radiation is integrated over the entire spectrum available to many commercial IR detectors. The same technique was employed in Refs. [40, 41], where the effect of the Marangoni instability on the film topology was investigated over a range of (locally applied) heat fluxes for $Re = 300$ and $Re = 500$ flows. A similar experimental arrangement was used in Ref. [42], in order to study the formation of a "hump" upstream of the heater, and its evolution to a rivulet pattern above a critical heat flux at the limit of negligible inertia (i.e., at $Re \approx 1$). In addition to interfacial temperature measurements, the authors also reported on interfacial velocities which they recovered by tracking the motion of buoyant Aluminium particles using a high-speed camera. Their measurements revealed a highly 3-D velocity field, with stagnation regions forming upstream of the "horseshoe-shaped" thermal features. More recently, Chorogiannis et $al.$ [43] demonstrated a thermographic velocimetry (TPV) technique capable of recovering simultaneously temperature and velocity information from the gas-liquid interface of falling-film flows using highly reflective (in the IR) silver-coated particles [43].

Combined interface-temperature and film-height measurements were also presented by Rietz et $al.$ [44] and Lel et $al.$ [45, 46] who investigated the interaction between hydrodynamic waves and thermocapillary forces in vertically falling, high-Ka, low-Re (< 20), high-Pr ($= 57 − 167$) silicon-oil flows. In greater detail, the authors of these publications reported the formation and development of quasi-regular thermal structures in laminar falling films and pro-vided experimental evidence on the thermocapillary nature of these structures. Finally, IR was used alongside a film-height measurement probe in experiments focusing on the development of Marangoni flows and the shrinkage characteristics of heated falling-films [47, 48]. In greater detail, Zhang and co-workers linked the contraction of the film in the spanwise direction of the flow, the formation of rivulets and the evolution of the film height with increasing streamwise distance from the flow inlet with the flow Re and the temperature at the solid-liquid interface.

We now proceed to discuss optical velocimetry techniques which typically utilise particles or molecular markers (dyes) for tracking the fluid motion. Examples of the former include PIV/PTV and laser Doppler velocimetry (LDV), whereas molecular tagging velocimetry (MTV) and photochromic dye activation (PDA) fall under the latter category. Both MTV and PDA, the latter being an adaptation of the former (see Ref. [4]), utilise phosphorescent molecules which produce a long-lived emission. MTV has found applications mainly in gaseous-flow investigations, where it is often used for simultaneous temperature measurements (see, for example, Ref. [49]), while PDA has been employed in a range of multiphase flows, including laminar [50] and turbulent falling-film flows [51] and counter-current annular flows [52], as it allows for direct visualization and measurement of velocity profiles. In contrast, velocimetry techniques that rely on particle seeding utilise the scattering signal or the fluorescence emitted by purposefully seeded or naturally occurring particles, or other flow-features such as micro-bubbles, within the probed fluid-volume. LDV relies on a measurement of the Doppler shift between the incident and scattered light from seeded particles and allows for highly localised velocity measurements (see, for example, Ref. [53] where local spanwise and streamwise velocities were recovered by employment of back-scattering LDV), while PIV and PTV track the motion of particle groups or individual particles, respectively, by sequential illumination and imaging of the scattering or fluorescence signals within a short time-step.

The employment of PIV/PTV in film-flow investigations has gathered momentum in recent years despite the restricted fluid domains under observation and the strong velocity gradients that are encountered across the often sub-millimetric film-height. Amongst the earliest applications of particle-seeded velocimetry is the study by Alekseenko et $al.$ [54], who combined film-height and velocity measurements in liquid falling films flowing down a vertical plane, using the shadow method and stroboscopic particle visualization, respectively. This combined optical technique allowed the authors to recover, for the first time, velocity profiles along the wave topology. More recently, the same group generated flow-field measurements in low-Re films forming pendant droplets underneath an inclined cylinder [55]. Based on these, the authors identified vortices in a reference frame moving with the wave speed, which were later shown to be inherent to pendant rivulets (see Rohlfs et $al.$ [56]).

The micro-PIV measurements of Dietze et $al.$ [57] provided the first experimental evidence of backflow (in the laboratory frame of reference) along the capillary ripples of liquid falling films flowing down a vertical plane. Later on, direct evidence of flow recirculation underneath the "humps"

of solitary waves were also provided by Reck and Aksel [58] for falling films flowing down a $10 - 15\,°$ incline with $Re = 15 - 20$. Adomeit and Renz [33] recovered instantaneous axial-velocity profiles in vertically-falling annular flows over the range $Re = 27 - 200$ using micro-PIV, and reported significant deviations from the Nusselt predictions despite the observation of parabolic profiles throughout their experiments. The same observation was reported by Moran *et al.* [50], who investigated the hydrodynamics of liquid films flowing down a $45\,°$ incline over the range $Re = 11 - 220$, this time using PDA. Zadrazil and Markides [24] employed PTV in their study of the flow phenomena underlying gas-liquid annular flows and observed multiple recirculation zones underneath the disturbance waves. These zones were speculatively linked to the mechanism of liquid entrainment in the gas core. Finally, Ashwood *et al.* [25] and Schubring *et al.* [59] conducted micro-PIV measurements in upward annular and horizontal gas-liquid flows, respectively, and reported deviations between their mean velocity-profiles and the universal velocity profile.

1.3 Objectives and outline

Having provided a brief discussion of select experimental contributions dedicated to the study of flow and heat transfer phenomena underlying falling-liquid films, we proceed to the primary objectives of this contribution, which are to: (i) establish the experimental methodology we employ in order to recover simultaneously space- and time-resolved film-height, velocity and heat transfer data in falling-film flows; (ii) conduct an uncertainty analysis and present validation data in support of the efficacy and accuracy of the proposed technique; and (iii) provide wave/phase-locked averaged, as well as time-varying flow and heat transfer data across the range of examined film-flow conditions. These span three forcing (wave) frequencies, $f_w = 7$, 12 and 17 Hz and $Re = 18 - 66$. The heat flux is fixed at $\dot{q} = 2.5$ W cm^{-2}; however, film-height and velocity measurements were also carried out for the same f_w and Re but with $\dot{q} = 0$ W cm^{-2}, and are compared directly to the heated cases.

The use of a high glycerol-content (55% glycerol by volume) aqueous solution introduces several noteworthy effects: (i) it results in low-conductivity (low Re, high-Pr) thick film-flows, wherein the development of hydrodynamic and thermal rivulets on the film free-surface is largely suppressed; (ii) it gives rise to significant liquid viscosity variations (by approximately a factor of four) across the imaged liquid-domain which is expected to significantly impact the film topology and flow field compared to an equivalent isothermal flow; and (iii) it results in a liquid viscosity that decreases along the streamwise direction as the film extracts heat from the substrate, which therefore, becomes progressively thinner and accelerates so that the mean flow is conserved.

Before proceeding with a description of the experimental apparatus in the next section of the manuscript, we define here the primary dimensionless numbers of the flows we investigate. These include the flow Reynolds, Re, which represents a dimensionless ratio between the inertial and viscous forces, and is defined in terms of the characteristic flow velocity U, the characteristic flow dimension D and the liquid kinematic viscosity, ν_f,

$$Re = \frac{UD}{\nu_f}, \qquad (1)$$

the liquid Kapitza number, Ka, which represents the ratio between surface tension and inertial forces [60], and is defined in terms of the liquid surface tension, σ_f, the kinematic viscosity, ν_f, the density, ρ_f, the substrate inclination angle β, and the gravitational acceleration, g,

$$Ka = \frac{\sigma_f}{\rho_f \nu_f^{4/3} (g \sin\beta)^{1/3}}, \qquad (2)$$

and the liquid Prandtl number, Pr, which compares the momentum diffusivity to the thermal diffusivity and is expressed as,

$$Pr = \frac{\nu_f}{\kappa_f}, \qquad (3)$$

where κ_f stands for the thermal diffusivity of the liquid.

In Section 2, we proceed with a brief description of our flow circuit and heated test-section, followed by a detailed account of the optical arrangement and the three optical techniques we employ, in Section 3. In Section 4, we present and discuss our results on the interface topology (recovered by PLIF), the flow field (recovered by PTV) and the interface temperature (recovered by IR) of the examined film flows, and conclude our analysis with a presentation of quantitative, space- and time-resolved heat transfer information.

2 Experimental apparatus

2.1 Flow circuit

The flow rig we employ in this study is based on the facility we described in Refs. [6–8, 12, 13, 43], and is therefore only described here in brief. The working fluid circulates inside the closed flow-loop shown in Fig. 1. Downstream of the test-section, which is inclined at a (constant) angle $\beta = 20\,°$, the liquid is collected in a tank, and then pumped via a heat exchanger that extracts any heat imparted to it by the heating arrangement, to the oscillator-valve and then back into the test section. The cooling-water flow rate to the heat exchanger is operated using valve V1, allowing us to maintain a near-constant working fluid temperature of 22 ±0.5 °C.

The oscillator-valve unit is equipped with a bypass valve that allows a prescribed portion of the flow through a rotating throttle-valve, itself is driven by a DC motor. Thus, the rotational speed of the valve can be adjusted to the nearest rpm, allowing for accurate control of the frequency of the imposed flow-rate fluctuations. Downstream of the oscillator-valve unit, the two flow-components (steady and periodically-varying) are joined, and the total, time-varying flow rate is measured using an ultrasonic flowmeter (UF25B by Cynergy3 Components), with an accuracy of 3%. The output signal from the flowmeter is recorded in MATLAB, and the amplitude of the flow rate fluctuations, which depends on the mean flow passing through V3, is calculated. This corresponds to $\approx 5 \pm 1\%$ of the mean flow-rate. Preliminary optical-measurement runs have shown that the main wave-characteristics (such as the wave-trough and crest heights) remain unaltered when the former is varied up
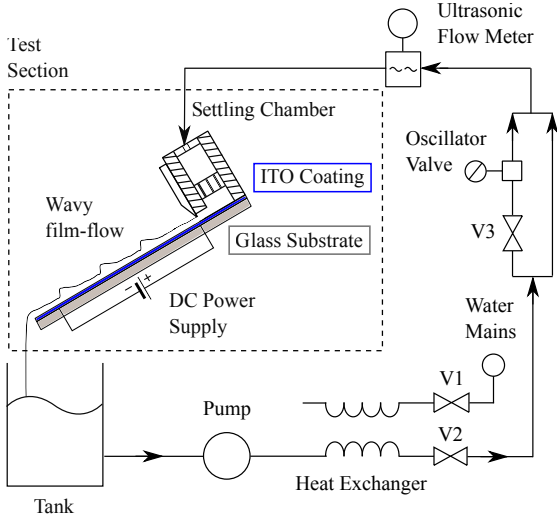
Figure 1: Schematic of the closed flow-loop showing the heated test-section, collection tank, pump, heat exchanger and flow-pulsation apparatus.

Table 1: Fluid properties of the employed water-glycerol solution at 22 °C, and flow and heating parameters of the experiment.

λ_f [Wm^{-1}K^{-1}]	0.37
κ_f [m^2 s^{-1}]	1.2×10^{-7}
ν_f [m^2 s^{-1}]	9.2×10^{-6}
σ_f [N m^{-1}]	60×10^{-3}
ρ_f [kg m^{-3}]	1.147×10^{-3}
$\overline{V}$ [m^3 s^{-1}]	$5 - 15 \times 10^{-5}$
β [°]	20
f_w [Hz]	7, 12, 17
$\dot{q}$ [W cm^{-2}]	0, 2.5
Re [−]	18 − 66
Ka [−]	180
Pr [−]	77

to $\approx$ 10%, at least when $\dot{q} = 0$ W cm^{-2}. Finally, a flow settling-chamber is installed at the film inlet in order to distribute the liquid evenly across the test section, and to dissipate any large-scale eddies and turbulence that is present in the pipes.

The kinematic viscosity, density and surface tension of the employed water-glycerol solution were determined experimentally using test samples that were collected during the optical-measurement runs. Multiple samples were collected in order to confirm that no significant surface-tension variations ensued due to exposure of the employed liquid to the laboratory environment (and its potential contamination with dust or other particles that could act as surfactants), and also to monitor any variations in the liquid viscosity due to water evaporation. An Attension Sigma 700 force tensiometer equipped with a Wilhelmy plate was used to measure the surface tension of the collected samples, which amounted to $\sigma_f = 60 \times 10^{-3}$ N m^{-1} at 22 °C. The standard deviation of the surface tension measurements, based on the 8 samples that were used to measure the other liquid properties as well, was < 3%. The mean value is lower than the surface tension of both water and glycerol, and in excellent agreement with our previous measurements (see Ref. [7]). Thus, the observed reduction of the liquid surface-tension can be attributed to the effect of the fluorescent dye and the particles, which have been reported to impact the surface tension of water-rich solutions.

The kinematic viscosity and density of the employed liquid were also measured, the former using a Poulten Selfe & Lee U-tube viscometer, and the latter using an electronic scale. The viscosity corresponds to $\nu_f = 9.2 \times 10^{-6}$ m^2 s^{-1} $\pm 2\%$, which suggests that any loss of water due to evaporation was insignificant. The density, $\rho_f = 1147$ kg m^{-3}, measurement was reproduced amongst the collected samples to within 0.25%. In contrast to the viscosity, density and surface tension, the liquid thermal conductivity, $\lambda_f = 0.37$ Wm^{-1}K^{-1}, and thermal diffusivity, $\kappa_f = 1.2 \times 10^{-7}$ m^2 s^{-1}, were estimated using the Fillipov equation in the first instance, and linear interpolation between values correspond-

ing to pure water and glycerol in the latter. Based on these, as well as the measured fluid-properties, a Prandtl number, $Pr = 77$, and a Kapitza number, $Ka = 180$, are reported. The liquid flow-rate was varied in the range $\overline{V} = 5 - 15 \times 10^{-5}$ m^3 s^{-1}, which results in $Re = 18 - 66$. The fluid properties of the employed water-glycerol solutions, and the flow and heating parameters of the experiment are summarised in Table 1.

2.2 Test section

The test section comprises a perspex frame on which the flow substrate is installed. The latter measures 300×300×1.1 mm and is made of soda-lime glass with its top surface (the side in contact with the liquid flow) coated with a thin, electrically-conductive indium tin oxide (ITO) layer. Two electrodes are established along the edges of the coated side of the substrate and are connected to a programmable, 5.5 kW DC-power supply that was manufactured by Magna-Power Electronics. The resistance of the coated glass corresponds to 4 Ω; thus, in order to achieve the intended heat flux of $\dot{q} = 2.5$ W cm^{-2}, the applied voltage and current were set to $\approx$ 100 V and $\approx$ 25 A, respectively. The optical transmittance of the glass in the visible is 0.85 according to the manufacturer (Optical Filters Ltd).

Prior to conducting the optical measurements, the heat loss due to natural convection from the bottom side of the test section (the side that not in contact with the liquid) was determined experimentally. Towards that end, a foam insulator was placed on the top side and the temperature at the downstream location where optical measurements were conducted was measured using K-type thermocouples, while small amounts of power were applied. The results from this study are presented in Fig. 2, where the difference between the ambient temperature, $T_\infty \approx 25$ °C, and the wall (substrate) temperature at the coated side of the substrate, $T_w = T_{ITO}$, and the uncoated side, $T_w = T_{glass}$, are plotted against the applied heat flux. The latter was increased
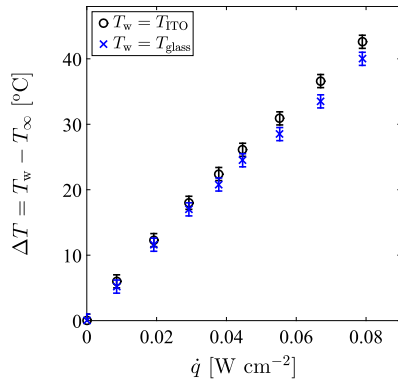
5

Figure 2: Temperature difference, $\Delta T = T_w - T_\infty$, between the heated glass-substrate and the ambient in the absence of a film flow, plotted against the heat flux applied to the test section, $\dot{q}$.

in small increments until the highest measured T_{ITO} would match the highest T_{ITO} value we observed in the film-flow experiments (i.e., $T_{ITO} \approx 60\,°C$). According to our findings, a heat flux of $\dot{q} \approx 0.08\ \mathrm{W\,cm^{-2}}$ (i.e., $\approx 73\ \mathrm{W}$) suffices to reach this temperature, which corresponds to a heat loss of $\approx 3\%$. This is accounted for when we quote the heat flux applied to the liquid film.

Additional tests were conducted in order to verify that the voltage distribution, and thus the heat-flux distribution, was uniform over the glass surface. These include point measurements using a multimeter, as well as temperature-distribution measurements using the IR camera, the latter during both dry tests, as well as tests with a film flow established over the plate. In both cases, any non-uniformity (described by the standard deviation of the measurements) was of the order of measurement noise.

3 Measurement methods

3.1 Optical arrangement

A pair of HS 500 CMOS cameras were used for PLIF and PTV, along with a frequency-doubled Litron Nd:YAG laser with a peak emission at 532 nm, while a FLIR X6540SC IR camera (640×520 pixel, InSb detector, spectral range of $2.5-5\,\mu m$) was used for the IR measurements. A photograph of the three-camera arrangement is presented in Fig. 3(a), alongside a schematic diagram showing the orientation of the PLIF and PTV cameras relative to the excitation plane when the test section is viewed from top in Fig. 3(b), and a schematic diagram showing the orientation of the PLIF, PTV and IR cameras relative to the excitation plane when the test section is viewed from the front in Fig. 3(c).

The PLIF and PTV cameras were located underneath the test section in order to visualise a small region of the flow from the flat, solid-liquid interface, thus preventing any time-varying optical distortions that would otherwise ensue if imaging was carried out through the wavy, gas-liquid interface. The angle between the imaging and excitation planes in the cross-stream direction of the flow was set to $35\,°$ in order to enhance the resolution of the collection optics and suppress any total internal reflection of the emitted fluoresce by the gas-liquid interface. The PLIF cam-

era was positioned at right angles to the excitation plane in the streamwise direction of the flow, while the PTV camera was slightly tilted, and was therefore equipped with a Scheimpflug adaptor. Both cameras were equipped with Sigma 105 mm f/2.8 Macro lenses and 24-mm extension rings in order to achieve the desired magnification. A short-pass optical filter with a cut-off frequency at 550 nm was installed on the PTV camera in order to block the fluorescence emitted by the dye-seeded liquid, while a long-pass filter with a cut-off frequency at 540 nm was installed on the PLIF camera in order to suppress any scattering signal by the particles. Rhodamine-B was used for PLIF at a concentration of $\approx 0.5\ \mathrm{g\,L^{-1}}$, while glass hollow-spheres of 11 μm mean diameter were seeded for PTV, at a concentration of approximately $0.2\ \mathrm{g\,L^{-1}}$.

The light produced by the Nd:YAG laser was directed to the sheet optics which were also installed underneath the test section in order to prevent any beam stirring and lensing effects. The sheet optics were used to generate a $\approx 250\ \mu m$ thick laser-sheet which extended along the test section in the streamwise direction of the flow, and through the middle of the film span. The laser was operated at a frequency of 100 Hz and was synchronised with the PLIF, PTV and IR cameras using a LaVision High Speed Controller and the LaVision Davis software. The imaging planes of the PLIF and PTV cameras were mapped at the imaging region, which extends between $x = 232$ mm and $x = 265$ mm downstream of the flow inlet, using a calibration graticule which was immersed in the employed water-glycerol solution, and the pinhole-camera model which is available in LaVision Davis. The spatial resolution of the PLIF/PTV measurement corresponds to $\approx 28\ \mu m/pixel$.

A calibration target comprising a highly-reflective metal mesh backed with black carton was used to locate the PLIF/PTV imaging region in the field of view of the IR camera, obtain the spatial resolution of the IR-camera measurement, and correct the raw IR images for perspective distortions. This was necessary as the camera was positioned at a slight angle to the test section in order to prevent it from capturing a reflected (by the gas-liquid interface) thermal image of itself. The camera was equipped with a 25 mm lens, which allows thermal radiation to be collected over the $2.5 - 5.0\ \mu m$ band in the mid-wave IR. Perspective distortion corrections were performed in LaVision Davis using the same methodology that was used with the PLIF/PTV cameras. Owing to the available optics, the spatial resolution of the IR camera (196 $\mu m/pixel$) was lower than that of the PLIF/PTV cameras, and therefore, the IR images were resampled using an anti-aliasing, finite impulse response (FIR), low-pass filter. The field of view of the IR camera was, however, considerably larger, spanning the region $x \approx 170 - 300$ mm downstream of the flow inlet.

3.2 Optical techniques

3.2.1 Planar laser-induced fluorescence

Both PLIF and PTV cameras were operated in dual-frame mode, as the location of the two interfaces was first identified in the former and then used to mask out any particle reflections in the latter. The time-delay between successive
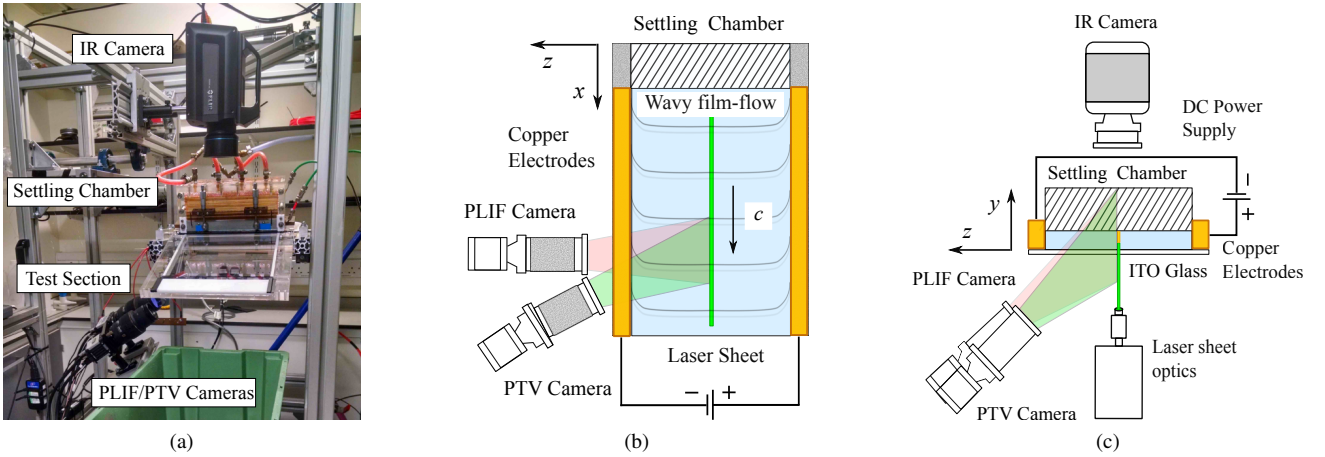
Figure 3: (a) Photograph of the heated test-section and three-camera arrangement. (b) Schematic of the test-section showing the relative orientation of the PLIF and PTV cameras, and the laser-sheet from above. (c) Schematic of the test-section showing the relative orientation of the PLIF, PTV and IR cameras, and the laser-sheet from the front. This figure was reproduced from Fig. 2 in Ref. [61].

frames was varied in the range $dt = 0.5 - 1.2$ ms depending on the flow Re, such that the particle displacement at the interface was ≈ 8 pixels. For each examined flow/heating condition, a total of 500 double-frame PLIF/PTV images were collected, which corresponds to a recording duration of 5 s.

In Fig. 4(a), we present a (perspective-distortion corrected) fluorescence image of a solitary wave from a flow with $\dot{q} \approx 2.5$ W cm^{-2}, $Re = 55$ and $f_w = 7$ Hz. Close inspection of this frame reveals several noteworthy features, the most prominent of which is a strong out-of-plane reflection between the wave crest and trough. This artefact originates from a total internal reflection of the fluorescence emitted locally by the excited liquid [36]. Second, a weak reflection of the emitted fluorescence about the gas-liquid interface and the glass surface blurs the fluorescence signal near the two boundaries of the flow. The emitted-fluorescence intensity is, however, significantly stronger (by approximately a factor of 7), and thus these reflections cause no ambiguity regarding the location of the two interfaces. More details on the artefacts that appear in the PLIF/particle images can be found in Ref. [7]. Finally, the fluorescence intensity along the thinner, hotter film-region preceding the main wave hump is considerably lower than the fluorescence emitted at the wave crest and along the gently-sloping back of the wave. This observation can be attributed to the strong temperature-sensitivity of the fluorescence emission of Rhodamine B, which corresponds to -1.59% °C^{-1} over the range $20 - 60$ °C according to Sutton *et al.* [29], and to -1.5% °C^{-1} according to our own measurements, over the range $10 - 40$ °C (see Ref. [13]).

The locations of the two interfaces were determined according to the methodologies described in Refs. [7–9], which were implemented using in-house developed algorithms in MATLAB. Briefly, the signal level corresponding to the solid-liquid boundary was calibrated against PTV measurements where the location of the wall was obtained according the no-slip condition. Any effects that the variation of the refractive index may have on the film-height and velocity measurements are discussed in the next section. Regarding the identification of the gas-liquid interface, we employed the gradient method described in Ref. [7] and estimated its location based on the intercept between a linear fit through the maximum PLIF-signal gradient, and a linear fit through the reflection intensity profile. This methodology was implemented on a per image-column basis, and was little affected by variations in the intensity of the reflected fluorescence emission outside the regions that were affected by total internal reflection. The erroneous film-height measurements that ensued in those regions were identified during post-stressing, and were interpolated using a smoothing-spline (for more details see Ref. [7]). A fully-processed PLIF image, also showing the location of the two interfaces, is provided in Fig. 4(b).

3.2.2 Particle tracking velocimetry

Binary "masks" were generated based on the PLIF images in order to be used for processing the simultaneously collected particle-scattering images. The masks are 2-D frames where the liquid domain is attributed a signal intensity equal to unity, and all other regions are set equal to zero; thus, any out-of-plane reflections in the particle images could be eliminated. The masked particle-images were then used to generate 2-D velocity-vector maps by means a PIV algorithm available in LaVision Davis, which utilised a four-pass cross-correlation for the calculation of the velocity field. The correlation-window size and the overlap parameter were set to 32×32 pixels and 50%, respectively, for the first two passes, and to 16×16 pixels and 50% for the last two.

A series of processing steps were applied during the initial passes, including the removal of any vectors that were calculated from a low cross-correlation peak (below 1.5), as well as any vectors that were calculated from particle groups containing less than 6 particles, and the application of median filtering for the removal of any spurious vectors. As a final processing step, the motion of individual particles (PTV calculation) was tracked using the PIV results as initial estimators of the velocity field. PIV and PTV velocity-vector maps corresponding to the PLIF frames shown in Fig. 4(a) and (b) are provided in Fig. 4(c) and (d). It should finally be noted that only the PTV maps were employed thereafter, for example for the calculation of local velocity profiles and
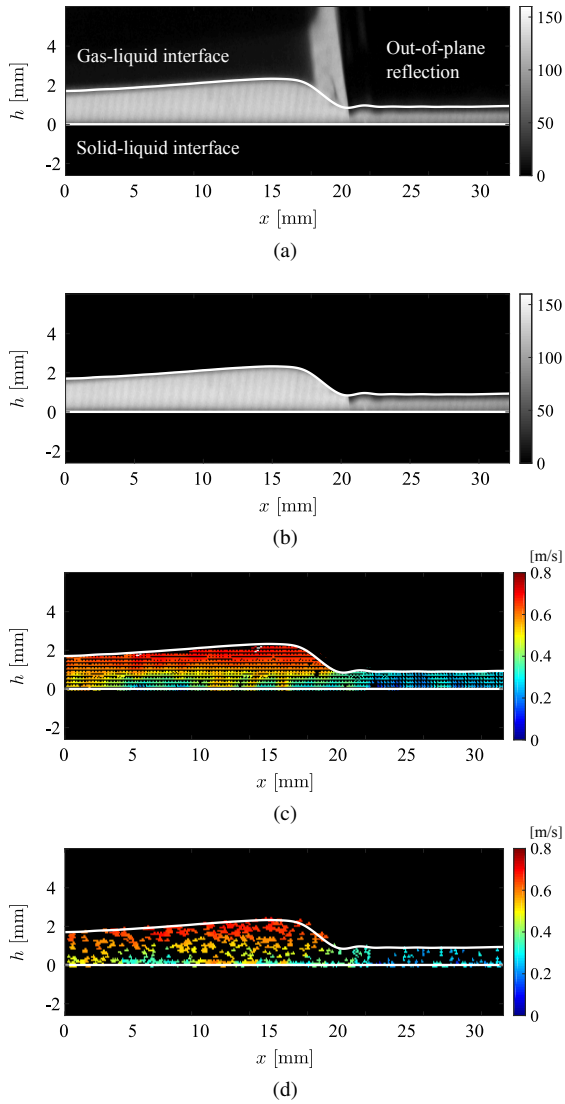
Figure 4: (a) Perspective-distortion corrected PLIF image of a solitary wave from a flow with $\dot{q} \approx 2.5$ W cm^{-2}, $Re = 55$ and $f_w = 7$ Hz. (b) Removal of reflections and identification of the gas-liquid and solid-liquid interfaces for the PLIF image shown in (a). (c) PIV velocity field for the PLIF frame shown in (a). P(d) PTV velocity field for the PLIF frame shown in (a).

bulk velocities, owing to the inherent limitations of PIV in flows with steep velocity-gradients and the superior spatial resolution on offer by PTV (for more details, see Ref. [7]).

3.2.3 Infrared thermography

A number of corrections were also applied to the raw IR-image sequences in order to convert the collected thermal-radiation measurements to 2-D, interfacial-temperature maps (see, for example, Fig. 5). This is feasible with the employed water-glycerol solution, as it is effectively opaque over broad IR-spectral bands; an attribute that allows for the collected thermal radiation to be integrated over very shallow ($\approx 10^{-5}$ m) optical depths. The transmittance of the water-glycerol solution over the spectral range of the FLIR IR camera (2.5 5 µm band) was measured using an FT-IR
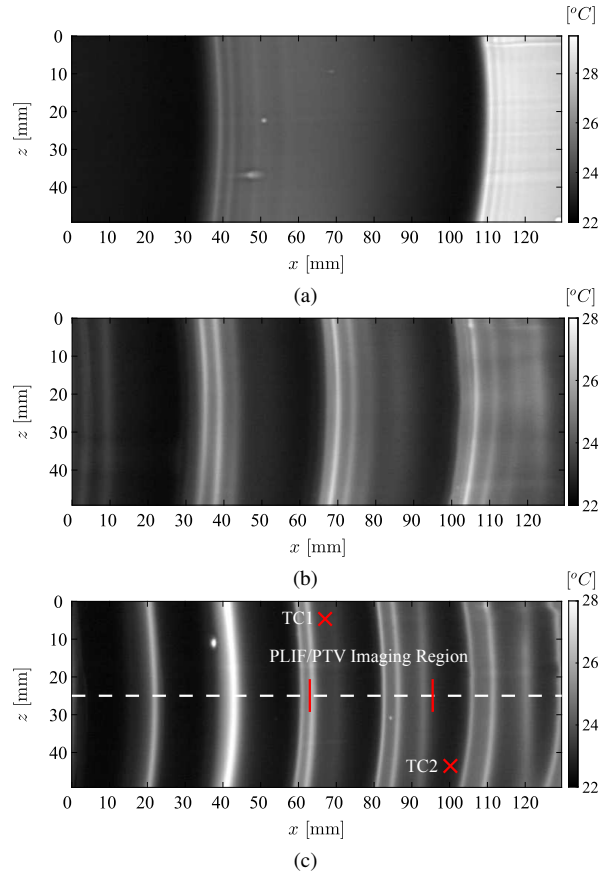

Figure 5: Instantaneous temperature distributions over the free-surface of falling-film flows with: (a) $\dot{q} \approx 2.5$ W cm^{-2}, $Re = 28$ and $f_w = 7$ Hz, (b) $\dot{q} \approx 2.5$ W cm^{-2}, $Re = 28$ and $f_w = 12$ Hz and (c) $\dot{q} \approx 2.5$ W cm^{-2}, $Re = 28$ and $f_w = 17$ Hz.

spectrometer (Perkin-Elmer Spectrum 100). Based on these results, an optical depth (i.e. the depth of the liquid over which the transmittance falls to $1/e \approx 37\%$ of the incident radiation) corresponds to < 60 µm. The thermal radiation collected by the camera, I_{meas}, comprised two contributions, the radiation emitted by the liquid and collected by the camera, $\epsilon_{li}I_{li}$, and any background radiation (i.e., any radiation emitted by the environment and reflected about the liquid surface and into the camera), $\rho_{li}I_{bg} = (1 - \epsilon_{li})I_{bg}$, such that

$$I_{meas} = \epsilon_{li}I_{li} + (1 - \epsilon_{li})I_{bg}, \tag{4}$$

where ϵ_{li} and ρ_{li} stand for the emissivity and the reflectivity of the employed water-glycerol solution, I_{li} for the thermal radiation emitted by the liquid surface, and I_{bg} for the background thermal radiation. The emissivities of water and glycerol correspond to ≈ 0.96 [62], and therefore, any contribution by the background was relatively limited. Yet, a correction was implemented using the camera software, ResearchIR, which necessitated a background temperature measurement. This was obtained by placing a flattened, crumpled piece of aluminum foil at the imaging plane and performing a temperature measurement with the emissivity set to $\epsilon = 1$. Finally, the thermal images were imported in LaVision Davis and corrected for perspective distortions, and later in MATLAB where they were converted to temperature measurements using the camera calibration corresponding to the selected frame integration period (843 µs).
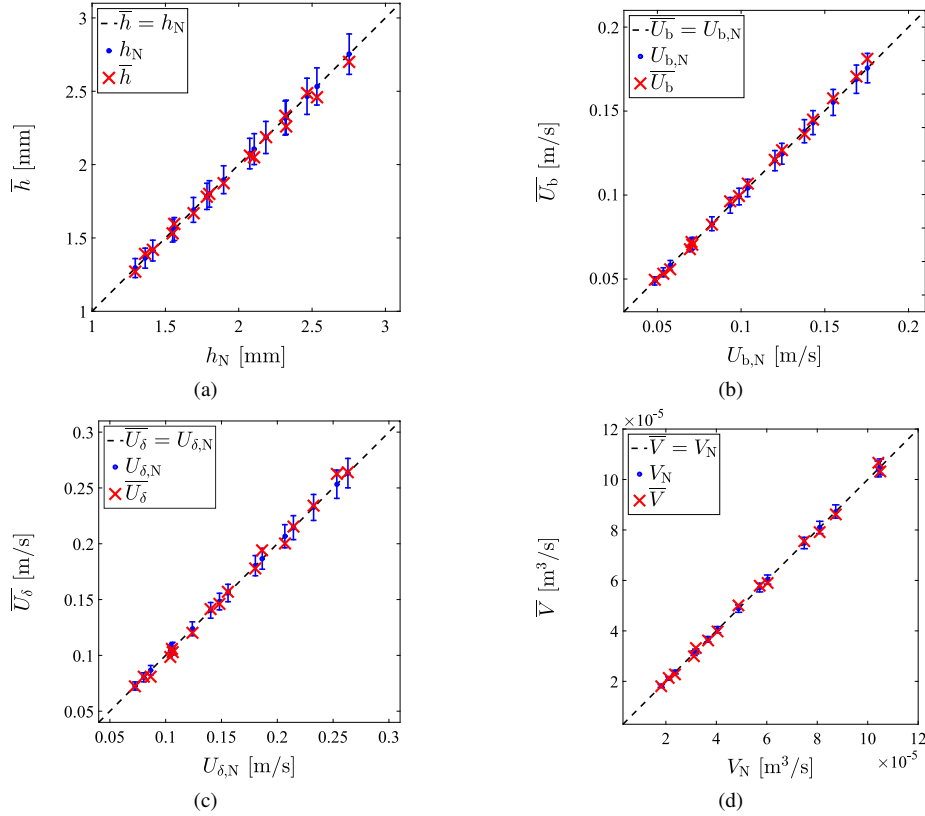
Figure 6: (a) Mean film-heights, $\overline{h}$, recovered by PLIF and plotted against calculated h_N data for 17 flat films spanning the range $Re \approx 1.5 - 11.5$. (b)-(c) Mean bulk and interface velocities, $\overline{U_b}$ and $\overline{U_h}$, recovered by PTV and plotted against calculated bulk and interface-velocities, $U_{b,N}$ and $U_{h,N}$, for the same film flows. (d) Mean flow-rates, $\overline{V}$, recovered using PTV and PLIF, plotted against the respective ultrasonic-flowmeter measurements, V_N.

The temperature-difference across the liquid film, and by extension the HTC, was recovered by measuring simultaneously the solid-liquid interface temperature along the PLIF/PTV imaging domain using two miniature K-type thermocouples (0.25 mm sheath diameter). These were attached using adhesive, thermally-conductive pads on either side of the PLIF/PTV imaging region and at a distance of ≈ 20 mm in the spanwise direction of the flow, along the top-most upstream and bottom-most downstream locations of that region (Fig. 5(c)). These coordinates were selected in order to prevent the thermocouples from perturbing the flow at the PLIF/PTV imaging region, but still be close enough to the latter so that the measured temperatures are representative of the solid-liquid interface temperatures along the excitation plane. This was verified in quality assurance runs, whereby multiple thermocouples were positioned at a downstream distance corresponding to the middle of PLIF/PTV imaging domain and at different spanwise locations. Further evidence in support of the validity of these measurements can be sourced from thermal images of the gas-liquid interface (such as the ones shown in Fig. 5), which indicate that the gas-liquid interface temperature varies by < 0.1 °C along the span of the IR measurement. Once the optical measurements were completed, the solid-liquid interface temperature along the PLIF/PTV imaging domain was obtained by linear interpolation between the two thermocouple measurements. The temperature difference along the PLIF/PTV imaging domain did not exceed ≈ 1 °C for the investigated heating and flow conditions.

3.3 Quality assurance and measurement-uncertainty estimation

3.3.1 Film-height measurements

Additional experiments were carried out in order to assess the validity and accuracy of the proposed, combined optical technique. For that purpose, the employed water/glycerol solution was replaced by a higher glycerol-content one ($\approx$ 80% glycerol by volume), with $\nu_f = 50 \times 10^{-6}$ m s^{-2}, $\sigma_f = 62 \times 10^{-3}$ N m^{-1} and $\rho_f = 1205$ kg m^{-3} at 25 °C. The liquid temperature was varied in the range $T_f = 24 - 30$ °, resulting in $Ka = 17 - 25$. The same liquid was also employed in earlier experimental studies of the hydrodynamic characteristics of isothermal falling-films in order to carry out validation experiments (see Ref. [7]), as any large-amplitude interface fluctuations are suppressed in the absence of flow pulsation. Thus, the film remains seemingly flat along the length of the test section, and the height, bulk velocity and interface velocity of the flow can be approximated with a high degree of accuracy using the Nusselt solution to the Navier-Stokes equation [63]. The latter assumes a gravity-driven, steady, fully-developed, 1-D flow, and results in the following analytical expressions for the film height, bulk velocity and interface velocity (Eqs. 5, 6 and 7, respectively):

$$h_N = \left(\frac{3 \nu_f^2 Re}{g \sin \beta} \right)^{1/3} \qquad (5)$$

$$U_{b,N} = \frac{g \sin \beta h_N^2}{3\nu_f} \qquad (6)$$

$$U_{h,N} = \frac{g \sin \beta h_N^2}{2\nu_f} \qquad (7)$$

By varying the liquid flow-rate and temperature, the flow Re was varied in the range $Re \approx 1.5 - 11.5$, resulting in Nusselt heights in the range $h_N \approx 1.3 - 2.5$ mm. These are plotted against the respective mean film-heights, $\bar{h}$, obtained by PLIF in Fig. 6(a). The error bars correspond to the upper bound of the uncertainty associated with the calculation of the Nusselt height (5%), which stems mainly from the flowmeter measurement-uncertainty (3%) and the uncertainty in the liquid kinematic-viscosity measurement (2%). The mean and root-mean-square (RMS) deviations between the predicted (i.e., h_N) and measured film-height values correspond to 1.3% and 1.6%, respectively. However, as thinner film-regions were observed in the investigated film-flows, a measurement-uncertainty of 2% is quoted for the averaged (time-averaged or phase-locked) film height measurements. Instantaneous and local film-height measurements are also subject to random errors originating mostly from camera noise, and are thus attributed a relative uncertainty of $4-5\%$, based on the calculation of the film-height standard deviation in flat-film runs.

3.3.2 Velocity measurements

We now proceed to examine the uncertainties associated with the calculation of the mean bulk and interface velocities, $\overline{U}_b$ and $\overline{U}_h$ respectively, from simultaneously collected PTV and PLIF images. The former were obtained by time-averaging instantaneous bulk velocities, U_b, that were each recovered from a single PLIF/PTV image pair. In greater detail, velocity data were averaged along a short (100-pixel) region of the flow in each image, thus yielding local axial-velocity profiles which were then integrated over the local film-height. The mean interface velocities were instead calculated using only velocity-profile data from near the gas-liquid interface.

At this stage it is essential to discuss the treatment of the near-wall data, which are subject to additional errors; specifically, particle reflections at the glass-substrate which bias the local axial-velocities towards higher values. In both the flat, as well as the wavy films, these artefacts affect film regions up to ≈ 250 µm away from the solid-liquid boundary (i.e., extending up to 17% of the examined flow fields, on average). This spatial extent is larger compared to our previous studies of isothermal film flows (where any affected regions only spanned $100 - 200$ µm), owing primarily to the lower transmittance and higher reflectance of the ITO-coated glass. In order to alleviate the relevant bias errors in the calculation of axial velocity profiles, the near-wall data were replaced by parabolic fits, with the axial velocity at the wall set to $U_w = 0$ m s^{-1}. For more information on the relevant procedure we refer the reader to Refs. [7, 8], where it is discussed in great detail. It should also be noted that this is a well-known, and largely unavoidable deficit of the application of PIV and PTV in similar flow-configurations [64].

Resuming the comparison between PTV-derived bulk and interface velocities, and those derived from the Nusselt solution, we calculated mean and RMS deviations of $\approx 1.7\%$ and

2%, and 1.7% and 3.3%, respectively. Our results are plotted in Fig. 6(b) and (c), with the error bars corresponding, once more, to the uncertainty associated with the analytical calculation of the two velocity components. These results are very satisfactory, especially considering that no systematic trends are observed, and that the majority of the measured data-points lie within the error bars. Additional validation was obtained by comparing mean flow-rate data, $\overline{V}$, obtained by combined PLIF/PTV, with flow-rate measurements that were recorded simultaneously using the ultrasonic flow-meter, V_N. The former were recovered by time-averaging instantaneous flow-rate measurements that were generated on a per-image basis, by multiplying the local film-heights with the local bulk-velocities. The mean and RMS deviations between the optical and flowmeter data are both below 3%, which coincides with the uncertainty associated with the flowmeter measurements.
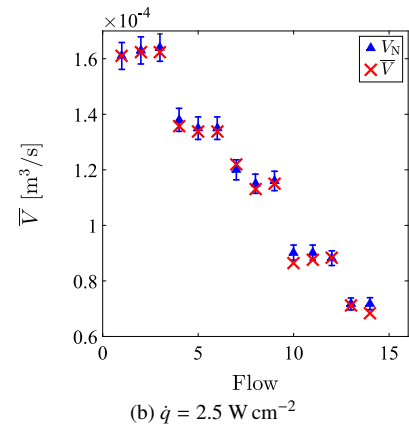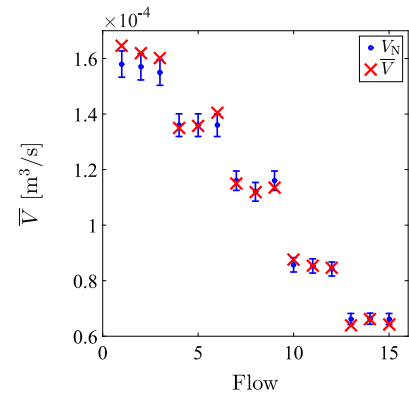

Figure 7: Mean flow-rates, $\overline{V}$, recovered using PTV and PLIF, plotted alongside the respective ultrasonic-flowmeter measurements, V_N, over the range $Re = 27 - 60$, for flows with: (a) $\dot{q} = 0$ W cm^{-2}, and (b) $\dot{q} = 2.5$ W cm^{-2}.

As a direct consequence of the high-viscosity water-glycerol solution we employ in our experiments, as the film heats up with increasing distance from the flow inlet, its viscosity decreases significantly. The film, therefore, becomes progressively thinner and accelerates so that the mean flow rate is conserved. In addition, based on our thermocouple and IR-camera measurements, the temperature difference between the two interfaces at the PLIF/PTV imaging region can attain values in the range $\Delta T \approx 30 - 40$ °C. According

to data provided by Cheng [65], the viscosity of our fluid decreases by $\approx 75\%$ between 20 and 60 °C; a variation that should mainly affect the velocity field near the wall, where the largest temperature gradients are encountered (i.e., at the region where our PTV measurements are discarded due to the presence of optical artefacts). In order to examine whether, and to what extent, this effect impacts our bulk-velocity measurements, we compare PLIF and PTV-derived mean-flow rate measurements with flowmeter measurements in wavy films, with and without heating. The former are plotted in Fig. 7(a), and the latter in Fig. 7(b), for 15 flow conditions spanning the range $Re = 27 - 60$.

In addition to the variation of the liquid viscosity with temperature, we also scrutinise the effect of the liquid refractive-index variation with temperature. Based on the measurements by Leron, *et al.* [66], the latter falls by $\approx 1\%$ over the same temperature range, and thus, its impact is expected to be moderate by comparison. The mean and RMS deviations between the PLIF/PTV-derived mean flow-rates and those measured using the ultrasonic flow meter, in the absence of heating, amount to 1.8% and 2.3% respectively, while the same values when a heat flux $\dot{q} = 2.5\ \mathrm{W\,cm^{-2}}$ is applied, correspond to 1.6% and 2.1% respectively. In both cases, the maximum absolute deviations do not exceed 5%. Based on these results, we are confident that neither the variation of the liquid viscosity near the wall, nor the variation of the liquid refractive index impact our bulk-velocity measurements, at least on a time-averaged basis.

3.3.3 Interface-temperature measurements

Finally, experiments were conducted in order to assess the accuracy of the IR-based, interface-temperature measurement. Towards that end, the rig was operated with the heat exchanger that is responsible for removing any heat imparted on the liquid, turned off (the flow-loop is described in greater detail Section 2.1, and illustrated in Fig. 1). As a result, the liquid flow was allowed to heat up uniformly and progressively over time, while IR and thermocouple measurements were collected simultaneously. Two K-type thermocouples were placed on either side of the $\approx 35 \times 35$ mm region of interest from which the IR-based temperature data were extracted, and their readings were averaged. Above $T \approx 33$ °C, additional heating was supplied using the heating arrangement in order to achieve the intended $20 - 40$ °C temperature range. The temperature measurements recovered using IR, T_{IR}, are plotted in Fig. 8 against the respective thermocouple measurements, T_{TC}. Based on these results, the measurement uncertainty of the IR measurement lies below 1 °C, with a probability $\geq 70\%$.

4 Results and discussion

4.1 Wave/phase-locked averaging and time-series generation

In this section, we introduce the application of wave/phase-locked averaging for the detailed study of the hydrodynamic and heat transfer characteristics of the quasi-periodic waves we observe in the experiments. In greater detail, we extract
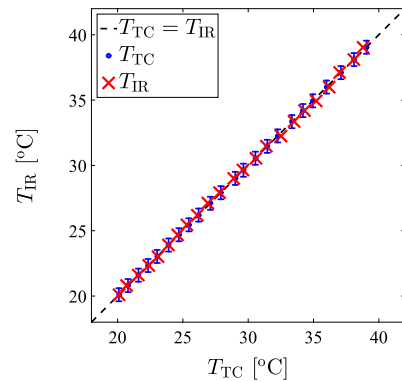

Figure 8: Gas-liquid interface temperature measurements recovered using IR, T_{IR}, plotted against simultaneously recovered thermocouple measurements, T_{TC}, over the range $T \approx 20 - 40$ °C.

highly localized film-height, velocity and heat-transfer data along the waves over a range of flow conditions, by application of the phase-locked averaging methodology we first presented in Ref. [7], and which we briefly describe here for completion. The first step comprises the selection of a reference image (i.e., an image of the wave topology of interest) and the identification of images from the same PLIF/PTV/IR recording, that will be averaged out. The latter are selected by cross-correlating the reference film-height with all other instantaneous traces from the same flow/heating condition; any traces that must be shifted by more than a prescribed translation threshold (in this case, 80 pixels) in order to match the reference topology are discarded, and the rest are shifted and averaged. Standard deviation calculations along the wave topology, which serve as qualitative uncertainty-estimators of the averaging procedure, are typically of the order of our film-height measurement resolution (around 30 μm), depending on the "waviness" of the film surface, as well as the number of signals that are averaged out. In isothermal flows, this number corresponds to around 80; however, when the flow is heated, the interface topology varies along the PLIF imaging region, which forces us to reduce the threshold translation, and thus utilize a smaller number of signals. A typical phase-locked average film-height measurement is provided in Fig. 9(a) for a flow with $Re = 51$, $f_{\mathrm{w}} = 17$ Hz and $\dot{q} = 0\ \mathrm{W\,cm^{-2}}$.

Using the information we obtain by cross-correlating the film-heights, we proceed to phase-lock average the respective velocity fields (e.g., Fig. 9(b)). From the latter, we can calculate the bulk velocity, U_{b}, along the wave topology by integrating the local axial-velocity profiles over the local film-heights, as well as the interface velocity, U_{h} (Fig. 9(c)). Finally, the local liquid flow-rate can be calculated by multiplying the local bulk-velocity with the film-height along the wave (Fig. 9(d)).

The same procedure (i.e. shifting and averaging) can also be applied to the interface-temperature measurements, as the image acquisition of the IR camera was synchronised with the PLIF/PTV image acquisition. Sample phase-locked average temperature measurements along the excitation plane are provided in Fig. 10, for flows with $Re \approx 28$, $f_{\mathrm{w}} = 7$, 12 and 17 Hz, and $\dot{q} = 2.5\ \mathrm{W\,cm^{-2}}$. The dotted lines repre-
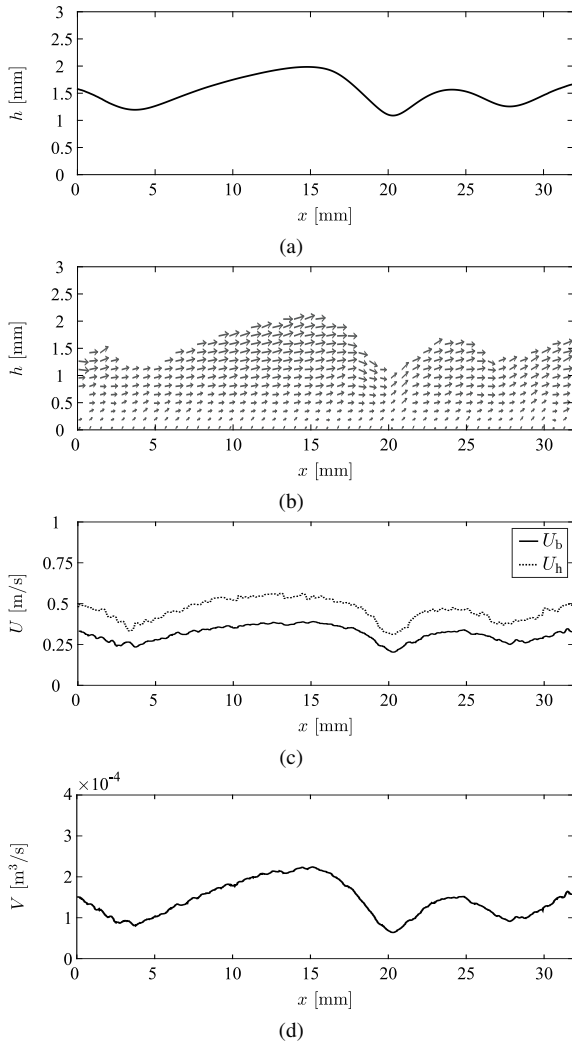
Figure 9: (a) Phase-locked average film-height, h. (b) Velocity field, (c) axial bulk and interface velocities, U_b and U_h, respectively, and (d) flow rate in the streamwise direction of the flow, V, for a flow with $Re = 51$, $\dot{q} = 0$ W cm^{-2} and $f_w = 17$ Hz.

capillary waves increase monotonically, unlike the interface temperature at the wave crests (two wave crests are observed in this phase-locked average measurement, at $x \approx 10$ mm and $x \approx 80$ mm) which remains almost constant and equal to the flow inlet-temperature. The variation of the interface temperature about the mean is limited.
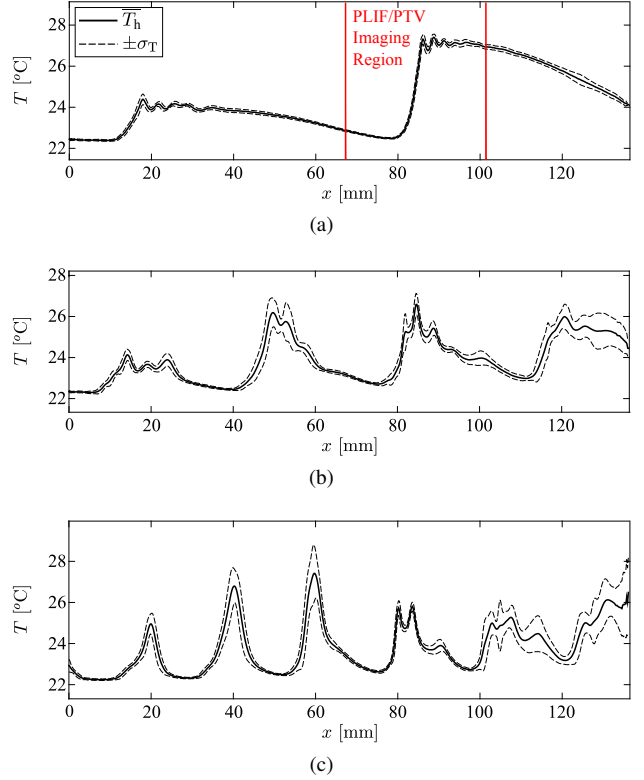

Figure 10: Phase-locked average gas-liquid interface temperature, T_h, from flows with $Re \approx 28$, $\dot{q} = 2.5$ W cm^{-2} and : (a) $f_w = 7$, (b) $f_w = 12$ Hz, and (c) $f_w = 17$ Hz. The flow region imaged by the PLIF/PTV cameras in Fig. 9 is shown in (a) in red, overlapping the T_h plots.

sent the standard deviation, $\pm\sigma_T$, of the average interface-temperature measurements. The $x = 0$ mm positions in Figs. 9 and 10 correspond to different distances from the flow inlet along the axial direction, as the data shown in each figure are collected using different cameras (PLIF/PTV and IR, respectively) with different fields of view and different spatial resolutions. Thus, they cover different spatial ranges along the heated test section. These ranges (also provided in Section 3) correspond to $\approx 232 - 265$ mm downstream of the flow inlet for the PLIF/PTV cameras, and to $\approx 170 - 300$ mm for the IR camera. In both figures, $x = 0$ mm signifies the start of the respective (i.e. for the PLIF/PTV cameras in Fig. 9 and for the IR camera in Fig. 10) imaged regions of the flow; however, as the flow region imaged by the IR camera is larger (≈ 130 mm) compared to the flow region imaged by the PLIF/PTV cameras (≈ 33 mm), the latter falls within the former, and is shown in red, overlapping the T_h plots in Fig. 10.

It is interesting to note that in the case of the $f_w = 7$ Hz flow, with increasing axial distance, x, the interface temperature along the thin substrate-film, the wave troughs and the

When the excitation frequency is increased to $f_w = 12$ Hz or $f_w = 17$ Hz, the interface temperature varies significantly at the wave troughs and throughout the capillary-wave regions in general, as evidenced by the locally higher σ_T (Fig. 10(b) and (c)). In the first instance (i.e., for $f_w = 12$ Hz), we observe that with increasing x, the temperature distribution evolves, possibly in response to variations in the interface topology which changes as the film heats up and the liquid viscosity decreases. Interestingly, the peak interface temperature is observed ahead of the third wave from the left, rather than the wave further downstream. This reduction of the peak interface-temperature with increasing distance from the inlet also relates to the $f_w = 17$ Hz flow. In greater detail, the temperature at the wave troughs increases consistently between $x = 0$ and 60 mm, as does σ_T over the first three waves; however, at the PLIF/PTV imaging region we observe two peaks of lower temperature than the peak value of the immediately preceding wave, while further downstream, T_h varies significantly and starts to climb along both the crests and troughs.

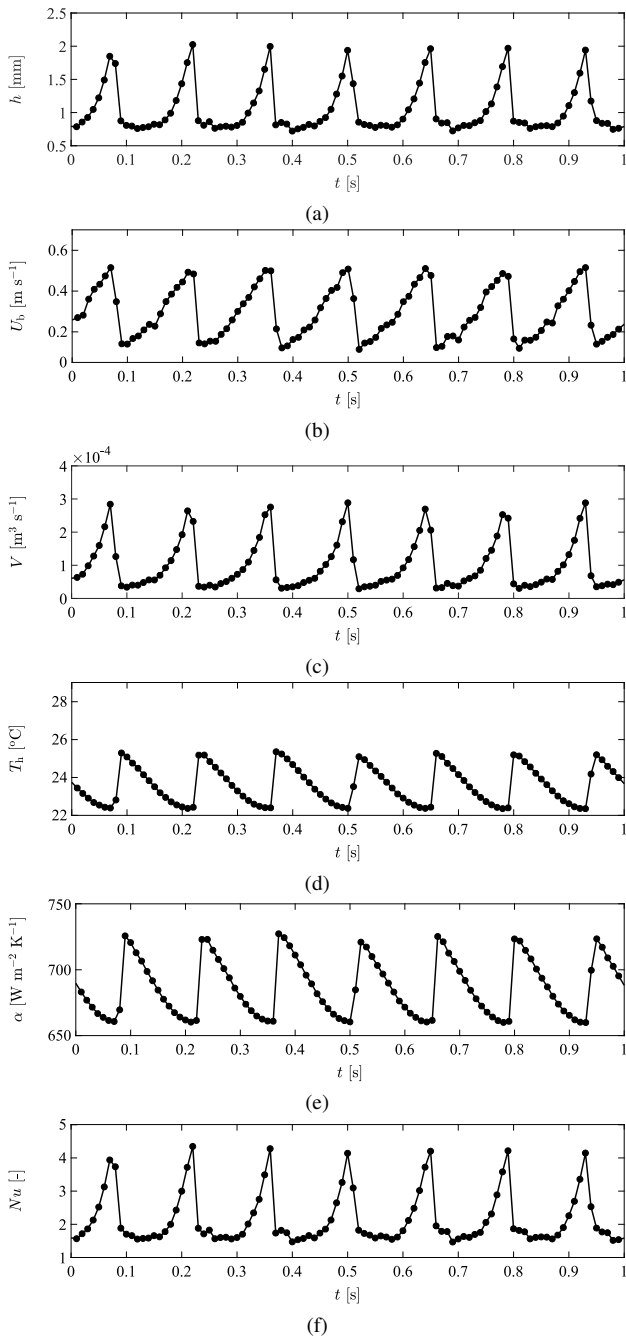Aside from the examination of the interface topology and

Figure 11: (a) Film-height, h, (b) bulk velocity, $U_{\rm b}$, (c) flow-rate, V, (d) gas-liquid interface temperature, $T_{\rm h}$, (e) heat transfer coefficient, a, and (f) Nusselt number, Nu, time series compiled over a 1-s recording period, for a flow with $Re = 35$, $f_{\rm w} = 7$ Hz and $\dot{q} = 2.5$ W cm^{-2}.

the velocity and temperature distributions by employment of phase-locked average data, the dependance of these quantities on the imposed flow and heating conditions were examined by employment of film height, bulk velocity, flow rate and gas-liquid interface temperature time-series (see, for example, Fig. 11, where we plot time-series of h, $U_{\rm b}$, V and $T_{\rm h}$ from a flow with $Re = 35$, $f_{\rm w} = 7$ Hz and $\dot{q} = 2.5$ W cm^{-2}). Time-varying film height data were generated by space-averaging the instantaneous film-heights over a 150-pixel ($\approx$ 4.2-mm) region of the flow, on a per image basis, while for the same flow region, bulk velocities were obtained by integrating the respective space-averaged axial

velocity profiles. In order to achieve a better compromise between accuracy and spatial resolution when the local film-topology is highly irregular, for example between the wave crests and troughs or along the capillary waves, the averaging domain was divided into three 50-pixel subdomains, yielding independent film height and bulk-velocity measurements which were then averaged.

Time-series of the heat transfer coefficient, a (Eq. 8), and Nusselt number, Nu (Eq. 9), were also generated using the obtained $T_{\rm h}$ and h data, respectively. Owing to the lack of bulk-temperature information, which would require a 2-D measurement of the temperature distribution across the liquid film, HTCs were calculated using the temperature difference ΔT between the gas liquid and solid liquid interfaces, and on the applied (mean) heat-flux, $\dot{q}$. The coupling between the observed variations in h, $U_{\rm b}$, V and $T_{\rm h}$ will be examined in the following sections, both locally as well as on a time-averaged basis; in the latter case based on statistical quantities that were determined using the time-series. Before proceeding, we would like to note that the pronounced similarity in the plots of $h(t)$ and $Nu(t)$ stems from the strong coupling between Nu and h which, in turn, can be attributed to the significantly larger variation (over time) of h compared to that of α in the examined, high-Pr liquid-films. This observation will be discussed in greater detail in Section 4.5, where the local and instantaneous variations of α and Nu are brought into focus.

$$\alpha = \frac{\dot{q}}{\Delta T} = \frac{\dot{q}}{(T_{\rm w} - T_{\rm h})}, \qquad (8)$$

$$Nu = \frac{\alpha h}{\lambda_{\rm f}}. \qquad (9)$$

4.2 Interface topology

In this section, we discuss the topology of falling films across the range of examined flow and heating conditions as a function of the flow Re and $f_{\rm w}$, based on phase-locked averaged film-height measurements in the vicinity of solitary waves (see Fig.12). Starting with the isothermal, $Re \approx 59$ flows, we observe that with increasing wave frequency, the wave crest-height falls whereas the through height remains almost unaltered. The solitary waves of the $f_{\rm w} = 7$ Hz flow are preceded by a single, low-amplitude capillary wave, while with increasing wave frequency, more capillary waves of longer wavelength and higher amplitude emerge. As the flow Re is reduced, first to $Re \approx 43$ and then to $Re \approx 25$, the solitary-wave crest and trough heights of all examined films fall. The number of capillary waves also falls, irrespective of the imposed $f_{\rm w}$; however, the amplitude of the remaining capillary ripples increases relative to the height of the main wave-humps and substrate film, as do their wavelengths. For the $f_{\rm w} = 17$ Hz case, the number of capillary waves falls from two to one and then they disappear altogether as the wave shape changes from the typical asymmetric hump with the steep front and long, flat tail, to a "sawtooth-like" shape. These observations are in good qualitative agreement with our previous work on flows with $\beta = 20$ ° and $Ka = 85 - 350$ (see Refs. [8, 9]).
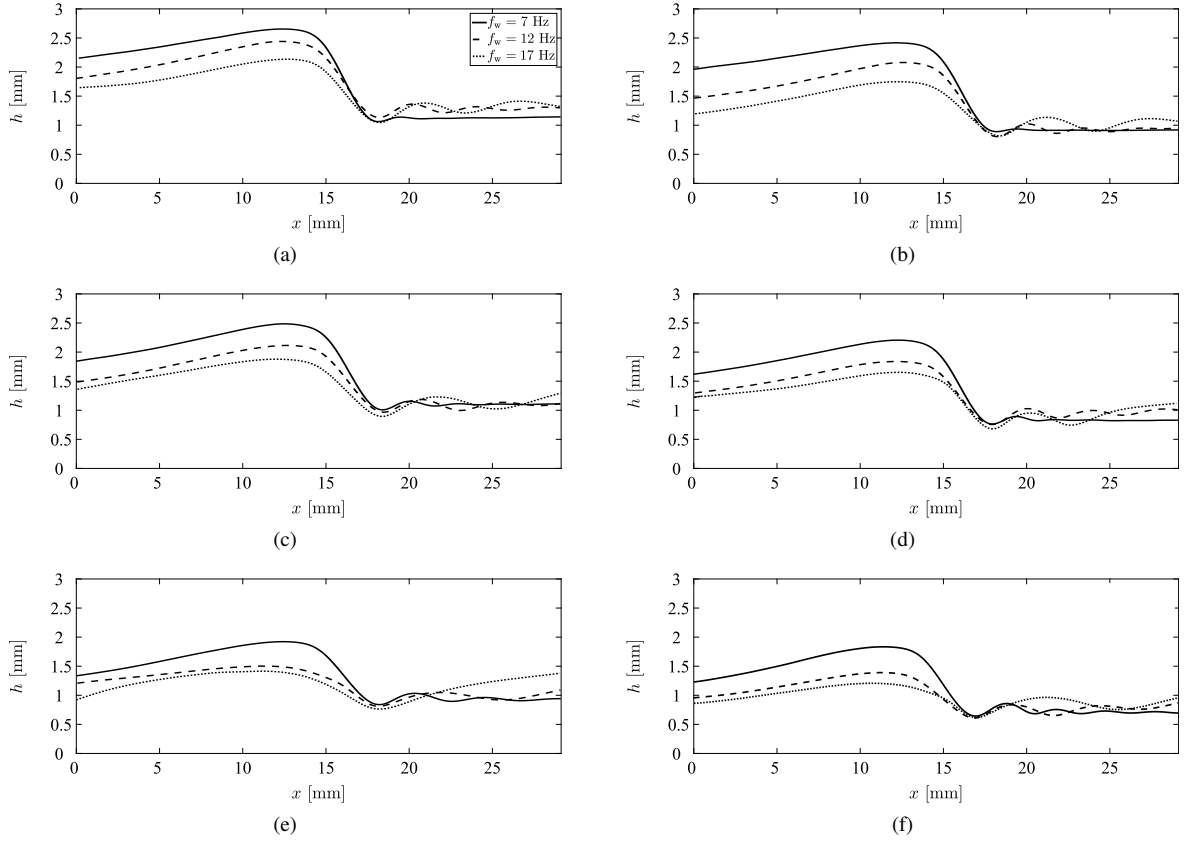
13

Figure 12: Phase-locked average film heights about the crests of solitary waves for flows with $f_w = 7$, 12 and 17 Hz, and (a) $Re \approx 59$ and $\dot{q} = 0$ W cm^{-2}, (b) $Re \approx 65$ and $\dot{q} = 2.5$ W cm^{-2}, (c) $Re \approx 43$ and $\dot{q} = 0$ W cm^{-2}, (d) $Re \approx 46$ and $\dot{q} = 2.5$ W cm^{-2}, (e) $Re \approx 25$ and $\dot{q} = 0$ W cm^{-2}, and (f) $Re \approx 28$ and $\dot{q} = 2.5$ W cm^{-2}.
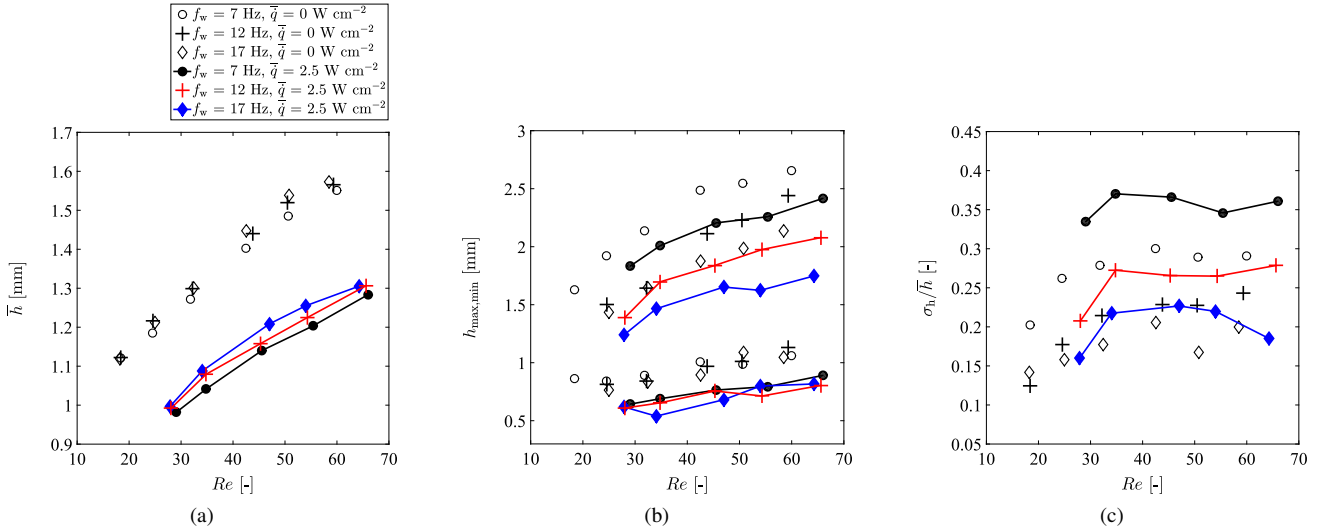

Figure 13: (a) Mean film-height, $\overline{h}$, (b) wave crest and tough-height, h_{max} and h_{min}, and (c) normalised standard deviation (coefficient of variation), $\sigma/\overline{h}$, data for flows with $Re \approx 18 - 65$, $f_w = 7$, 12 and 17 Hz, and $\dot{q} = 0$ and 2.5 W cm^{-2}.

When a heat flux $\dot{q} = 2.5$ W cm^{-2} is applied at the wall, the interface topology of the examined films over roughly the same Re range ($Re \approx 65 - 28$) displays some noteworthy disparity compared to their isothermal counterparts (i.e., flows with the same Re and f_w). The most discernible effect is a thinning of the flow in response to the reduced viscosity of the employed water-glycerol solution. Interestingly, the shapes of the waves are largely reproduced, with the ex-

ception of the $Re \approx 28$ and $f_w = 17$ Hz flow that is now populated by solitary, rather than sawtooth waves.

The mean film-heights, $\overline{h}$, wave crest and trough heights, h_{max} and h_{min}, and film-height coefficients of variation, σ_h/h_{max}, of all examined films are presented in Fig. 13 as a function of the flow Re. The mean film-heights we recover (Fig. 13(a)) increase monotonically with the flow Re and irrespective of the applied heat flux. When $\dot{q} = 2.5$ W cm^{-2},

14

these are, on average, $\approx 18\%$ lower compared to the equivalent isothermal cases, irrespective of the wave frequency and despite the fact that the heated film-flow data are collected at slightly higher Re. Interestingly, the disparity between the $\overline{h}$ data from the heated and unheated cases, and roughly the same flow Re, only varies between $\approx 16\%$ and 20%. The wave crest-heights lie $\approx 9\%$ lower, on average, when $f_w = 7$ Hz and $f_w = 12$ Hz, and $\approx 15\%$ lower when $f_w = 17$ Hz, while the wave trough-heights fall significantly more following the application of heating, by $\approx 25\%$ when $f_w = 7$ Hz and $f_w = 12$ Hz, and by and 21% when $f_w = 17$ Hz. Another interesting observation relates to the wave amplitude, which we define as $(h_{max} - h_{min})/\overline{h}$, and which is consistently higher for the flows with $\dot{q} = 2.5$ W cm^{-2} (for the same f_w and Re). Specifically, the wave amplitudes increase by $\approx 23\%$, 31% and 17%, on average, when $f_w = 7$ Hz, 12 Hz and 17 Hz, respectively. This result stems from the larger relative decrease of the mean and wave-trough heights compared to the crest heights.

The film-height standard deviations, σ_h, increase with the flow Re below $Re \approx 40$ for all examined wave frequencies, and then saturate at higher Re. The films with $f_w = 7$ Hz display the highest σ_h values, peaking at $\sigma_h = 0.46$ mm at $Re \approx 60$, due to the larger-amplitude waves that are encountered in these flows. These trends are in qualitative agreement with our earlier results on isothermal falling films [7–9], as well as the results by other researchers [50, 67, 68]. Following the application of heating, the recovered σ_h nearly match the isothermal cases, with the mean deviation between heated and unheated flows (of roughly the same flow Re) amounting to $\approx 10\%$. Consequently, the film-height coefficients of variation are consistently higher for the heated films, peaking at $\sigma_h/\overline{h} = 0.37$ for the $Re = 35$ and $f_w = 7$ Hz flow. In comparison, when $f_w = 12$ Hz, $\sigma_h/\overline{h}$ peaks at 0.27, at $Re = 34$, while when $f_w = 17$ Hz, $\sigma_h/\overline{h}$ peaks at 0.22, at $Re = 47$. It should finally be noted that the observed trends (i.e., the sharp increase of $\sigma_h/\overline{h}$ with increasing flow Re until a plateau is reached, as well as the higher $\sigma_h/\overline{h}$ at lower f_w) are shared amongst the isothermal and heated data.

4.3 Flow-field characterization

In our previous publications on the hydrodynamics of falling films (see Refs. [7–9]), we demonstrated the generation of axial velocity profiles at different locations along the waves, compared those to theoretical Nusselt-flow predictions, and commented on the topology-dependant under- and overestimation of the local axial velocities, bulk velocities and flow rates by the latter. Specifically, we noted that behind the wave crests, the measured profiles were always parabolic; however, the Nusselt predictions overestimated the measured velocities significantly (often by $\geq 100\%$). In contrast, between the crests and troughs and along the capillary waves, non-parabolic profiles were encountered, while ahead of the capillary waves, our bulk-velocities were higher (by $\approx 10 - 30\%$) than those suggested by the Nusselt theory. These observations, which are in excellent agreement with the work of other researchers (see, for example, Refs. [4, 33, 50]), also relate to the isothermal and heated falling-films we examine in this study.

In Fig. 14, we compare axial-velocity, U_x, profiles extracted in ≈ 1.55 mm intervals along the wave topology of films with $Re = 44$, $f_w = 12$ Hz and $\dot{q} = 0$ W cm^{-2} (shown in red), and $Re = 45$, $f_w = 12$ Hz and $\dot{q} = 2.5$ W cm^{-2} (shown in blue), with Nusselt profiles that were derived based on the local film-height of the isothermal flow (shown in black). The Nusselt predictions underestimate the experimentally-derived velocities between locations 1 and 3, agree well with the experimental data between locations 4 and 5, and then begin to increasingly overestimate the experiment (by up to 60% at the gas-liquid interface) between locations 6 and 11. Between the crest and trough of the wave, the measured U_x increase above the analytical values, while the observed profiles deviate from the typical parabolic-shape. Past the wave crest and along the capillary waves and the substrate film, the Nusselt velocities are once again lower than the measured values, by up to 30% at the free surface.

Regarding the heated-flow, the measured profiles appear consistently "fuller", but are still mostly parabolic excluding any regions where the interface slope is high, in agreement with the isothermal case. The observation of significant similarities between two flow fields is surprising, also considering that the flow-velocities near the wall were expected to be significantly higher for the heated cases. However, as the liquid temperature falls rapidly with increasing distance from the wall, and therefore the pronounced variation of the liquid viscosity is confined near the wall where our PTV measurements are subject to larger errors, a more thorough investigation of the relation between the local and instantaneous viscosity and flow rate is deemed necessary. This will be pursued by direct numerical simulations (DNSs) based on the methodologies of Denner *et al.* [69–71], from which the temperature and viscosity distributions across the waves will be extracted and linked to the local flow-fields, thus allowing greater insight into this complex flow behaviour. We would finally like to comment on the absence of regions along the investigated wave topology where the measured profiles match the Nusselt profiles. This is due to the lack of a true residual layer (substrate film) when $f_w = 12$ Hz, as the region bounded by locations $15 - 20$, for example, is populated by capillary waves and its right-most part already constitutes the tail of the preceding wave. In contrast, at lower f_w, for example when $f_w = 7$ Hz, a substrate-film region (where any film-height fluctuations are absent) can be observed, and the axial velocity profiles coincide with the Nusselt profiles. An example of this can also be found in our previous publication (see, Ref. [7].)

The variation of the mean bulk-velocity, $\overline{U_b}$, with the flow Re, the wave frequency and the heat flux are examined in Fig. 15(a). Both isothermal and heated flow datasets display the same trend; a near-linear increase with the flow Re. The bulk velocities that we recover in the heated flows are, however, 18% higher on average compared to the equivalent isothermal flows. When $\dot{q} = 2.5$ W cm^{-2}, the $f_w = 17$ Hz flows display slightly, yet consistently, higher $\overline{U_b}$, followed by the $f_w = 12$ Hz flows and finally the $f_w = 7$ Hz flows. In contrast, any deviations between the measured $\overline{U_b}$ (for the same flow Re) in the isothermal flows are smaller. Another noteworthy observation relates to rate of increase of the mean bulk-velocity with the flow Re, which is significantly higher than the rate of increase of the mean film-height with
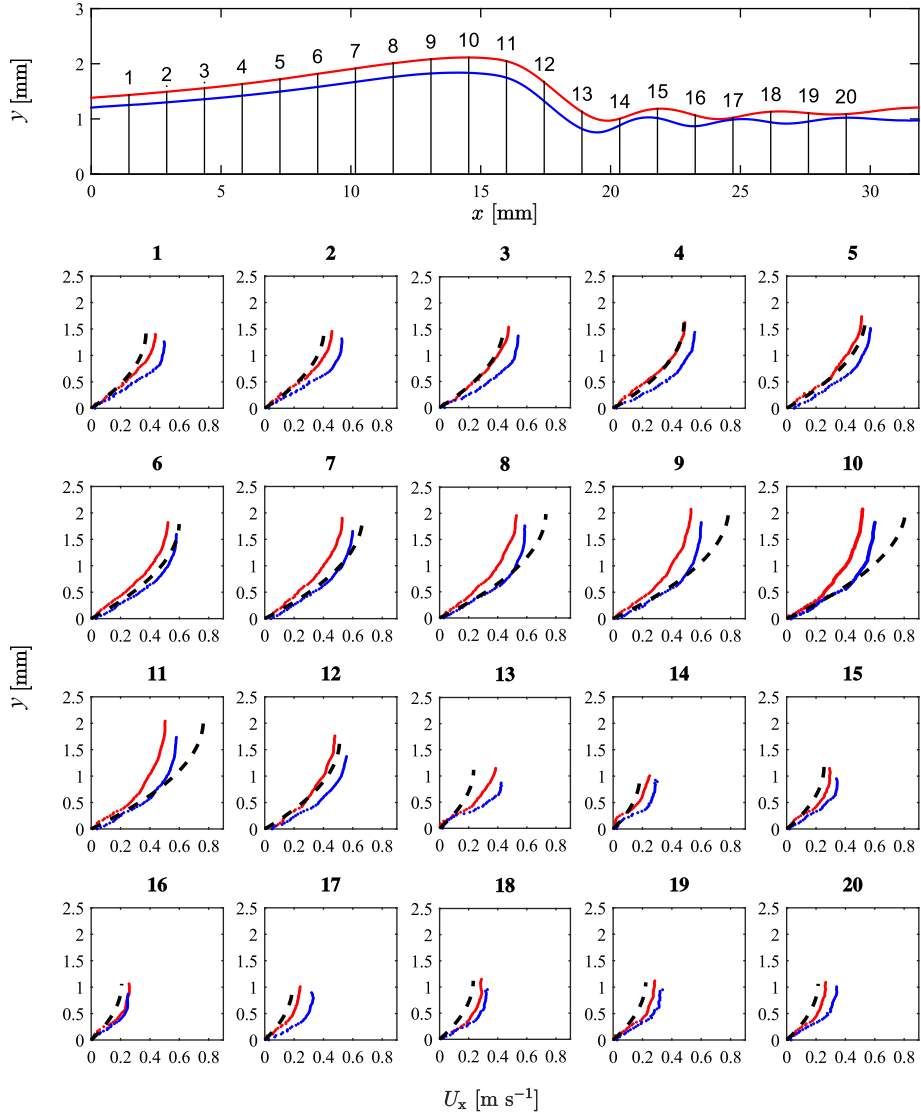
Figure 14: Phase-locked average wave-profiles for film flows with $Re = 44$, $f_w = 12$ Hz and $\dot{q} = 0$ W cm^{-2} (red trace), and $Re = 45$, $f_w = 12$ Hz and $\dot{q} = 2.5$ W cm^{-2} (blue trace), presented alongside axial-velocity profiles that were extracted in ≈ 1.55 mm intervals along the wave topology. Analytically derived (Nusselt) profiles are also plotted (black, dotted lines) based on the local film-height for the isothermal flow.
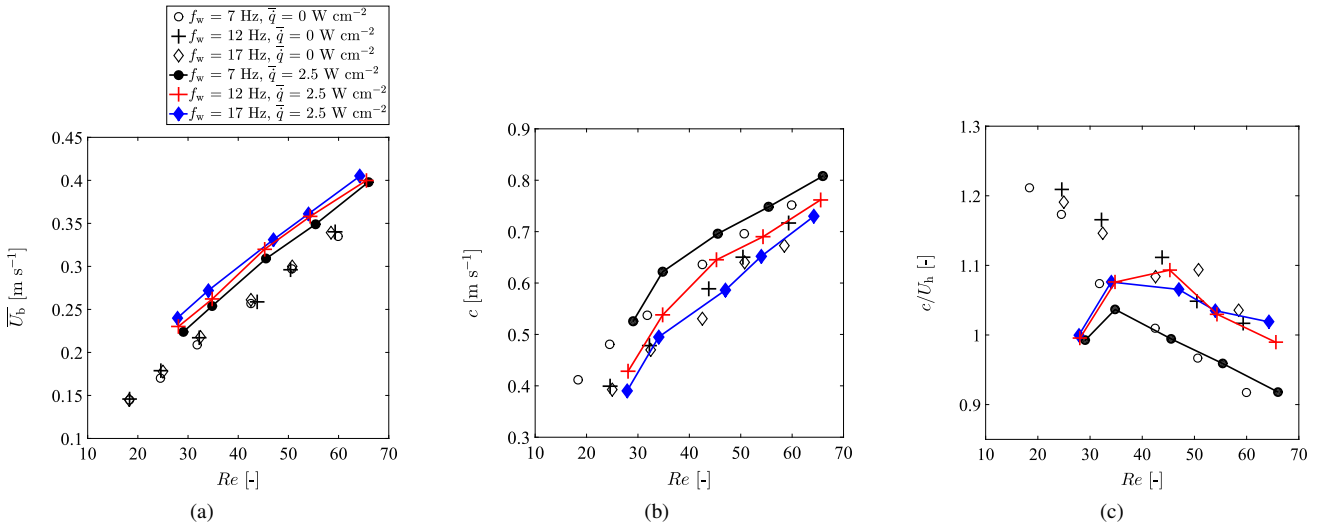

Figure 15: (a) Mean bulk-velocity, $\overline{U_b}$, (b) wave speed, c and (c) normalised wave speed (by the peak interface velocity, U_h) data for flows with $Re \approx 18 - 65$, $f_w = 7$, 12 and 17 Hz, and $\dot{q} = 0$ and 2.5 W cm^{-2}.

the flow Re. For example, over the range $Re \approx 20 - 60$ and for $f_{\mathrm{w}} = 17$ Hz and $\dot{q} = 0$ W cm^{-2}, $\overline{h}$ increases by $\approx 47\%$ whereas $\overline{U}_{\mathrm{b}}$ increases by $\approx 130\%$. This result stems directly from the observation of parabolic velocity-profiles, almost throughout the entirety of the examined film topologies.
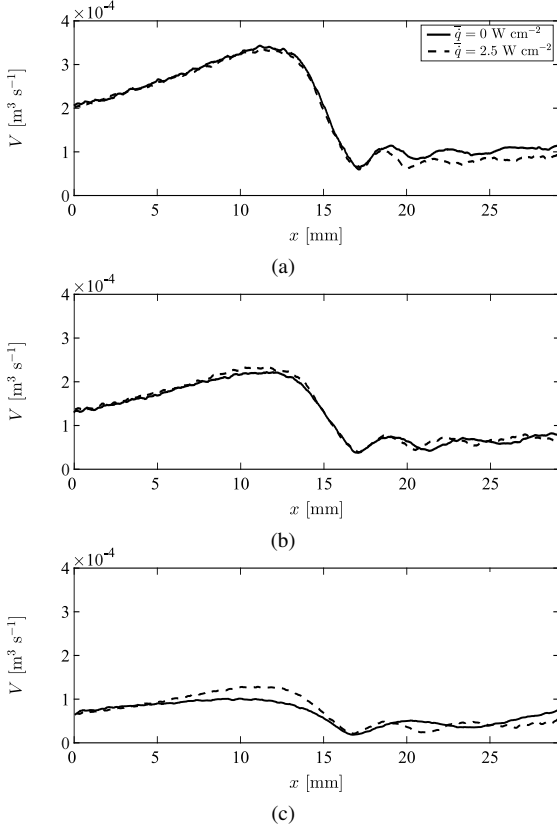

Figure 16: Phase-locked average flow-rates along the waves of flows with $f_{\mathrm{w}} = 12$ Hz, $\dot{q} = 0$ W cm^{-2} and $\dot{q} = 2.5$ W cm^{-2}, and: (a) $Re \approx 59 - 65$, (b) $Re \approx 43 - 46$, and (c) $Re \approx 25 - 28$.

Based on our previous discussion of the under- and overestimation of the local bulk velocities by employment of the Nusselt description of these flows, it is evident that U_{b} (i.e., the instantaneous bulk-velocity) does not scale with $\sim h^2$. Also, in Ref. [8], we showed that at least for isothermal falling-films, the instantaneous bulk-velocity is fixed by the magnitude of interface-height fluctuations and the mean flow. Before revisiting this result, this time in relation to the heated flows we investigate here (which is all the more interesting considering the strong variation of the liquid viscosity both along the test section, as well as across the thickness of the film), we plot phase/wave-locked average flow-rate distributions along the waves of flows with different Re, $f_{\mathrm{w}} = 12$ Hz and $\dot{q} = 0$ and 2.5 W cm^{-2}, in Fig. 16. Close inspection of the $Re \approx 43 - 46$ and $Re \approx 59 - 65$ data, and the respective film-height data shown in Fig.13, reveals that the former match near-perfectly from behind the wave crests and up to the wave troughs, irrespective of the value of $\dot{q}$. In contrast, along the capillary-wave region where the topology of the isothermal and heated film-flows is different, the flow-rate data do not match. The same remark can be used to describe to the flow-rates along the waves of flows with $Re \approx 25 - 28$, $f_{\mathrm{w}} = 12$ Hz and $\dot{q} = 0$ and 2.5 W cm^{-2}, which

display slightly dissimilar shapes.

In Fig. 15(b) we plot the wave speed, c, as a function of the flow Re over the examined flow and heating conditions. This data was recovered by first generating phase-locked averaged film-height measurements for the frames preceding and following those that were employed in our previous analysis (i.e., frames with the wave fronts located roughly at their centres). The displacements of the wave fronts were then calculated by cross-correlating the wave-regions between the wave crests and troughs, and the obtained results were divided by the dt between the frames, and averaged. Referring to the heated film-flows, it should be noted that the waves never develop fully over the length of our test section, as the liquid properties vary continuously in space.
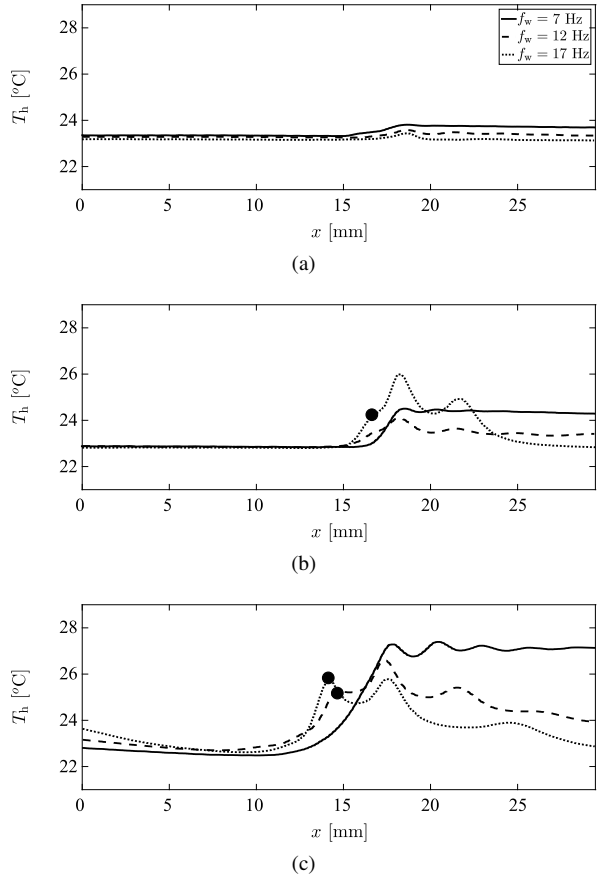

Figure 17: Phase-locked average interface temperature, T_{h}, along the waves of flows with $\dot{q} = 2.5$ W cm^{-2}, $f_{\mathrm{w}} = 7$, 12 and 17 Hz, and: (a) $Re = 66$, (b) $Re = 46$ and (c) $Re = 28$. The black dots in (b) and (c) mark the locations of local overshoots in T_{h}, in the regions bounded by the wave crests and troughs.

Resuming the discussion of our wave-speed results, we note that with increasing flow Re the wave speeds increase for all f_{w} and irrespective of the applied heat flux. In reference to the isothermal films, the cases with $f_{\mathrm{w}} = 7$ Hz display the highest wave-speeds (peaking at above > 0.75 m s^{-1} at $Re \approx 60$), followed by the $f_{\mathrm{w}} = 12$ Hz flows and then the $f_{\mathrm{w}} = 17$ Hz flows. This trend is attributed to the higher wave amplitudes that are observed at lower wave frequencies (see also Refs. [8, 10]). When $\dot{q} = 2.5$ W cm^{-2} we ob-

serve the same trend, as well as very similar wave-speeds to the isothermal cases. When normalised by the maximum interface velocities (corresponding to the velocities at the wave crests), however, some noteworthy differences arise. This comparison is presented in Fig. 15(c). Above $Re \approx 40$, the normalised wave speeds from the isothermal and heated cases all increase as the Re falls, while below that Re they display opposite trends. We speculate that the decrease in c/U_h is linked to the reduction in the liquid viscosity, and thus the faster flow velocities that ensue compared to the isothermal flows. Furthermore, in Fig. 12 we show that any topological changes (following the imposition of $\dot{q} = 2.5$ W cm^{-2} at the wall) are more pronounced for flows with $f_w = 12$ and 17 Hz, and that these include an increase of the observed wavelengths (Fig. 12(e) and (f)). The latter should bring about a reduction in c, provided that f_w remains constant.

4.4 Interface-temperature measurements

We now proceed to examine the variation of the gas-liquid interface temperature along the PLIF/PTV imaging region (Fig. 17). Specifically, we discuss the variation of T_h along the wave topology of flows with $f_w = 7$, 12 and 17 Hz, $Re = 28$, 46 and 66 and $\dot{q} = 2.5$ W cm^{-2}. The lowest temperatures are observed consistently at the wave crests, nearly matching the liquid inlet-temperature, $T_i \approx 22 - 23$ °C. The interface temperature upstream of the wave crests is little varied, increasing gradually as the film heights decrease. For the highest Re, the measured T_h display very little change downstream of the crests as well, as the heating applied at the wall does not penetrate through the thickness of the film. However, owing to the excellent sensitivity of the IR camera, a slight increase in T_h is observed in that region, tracking the shape of the interface.

The coupling between T_h and h is stronger when $Re = 46$, and the three temperature profiles display distinct shapes (Fig. 17(b)). Yet, T_h increases by only $1 - 3$ °C between the wave crests and troughs, peaking along the capillary waves. When $f_w = 7$ Hz, the interface temperature exhibits a maximum at the solitary-wave trough, and plateaus along the substrate film. This region of the film also exhibits a near-constant thickness, which lies well below the mean film-thickness. When $f_w = 12$ Hz, a similar behaviour is observed, though the increase in T_h at the wave trough is slightly smaller. The flow with $f_w = 17$ Hz displays the highest interface temperature, $T_h \approx 26$ °C, and a "step-like" increase in T_h in the sloping region between the solitary-wave crest and trough which is reproduced, and in fact is even more pronounced, when $Re = 28$ (Fig. 17(c)). Interestingly, for the same Re, this feature is also observed in the $f_w = 12$ Hz flow. The locations of these local overshoots in T_h, in the regions bounded by the wave crests and troughs, are marked in Figs. 17(b)-(c) and 18 with black dots. Finally, it is worth noting that despite the reduction in the flow Re from $Re = 46$ to $Re = 28$, the peak T_h is slightly lower for the $f_w = 17$ Hz flow. Instead, the highest T_h value is observed along the capillary-wave region of the $f_w = 7$ Hz flow.

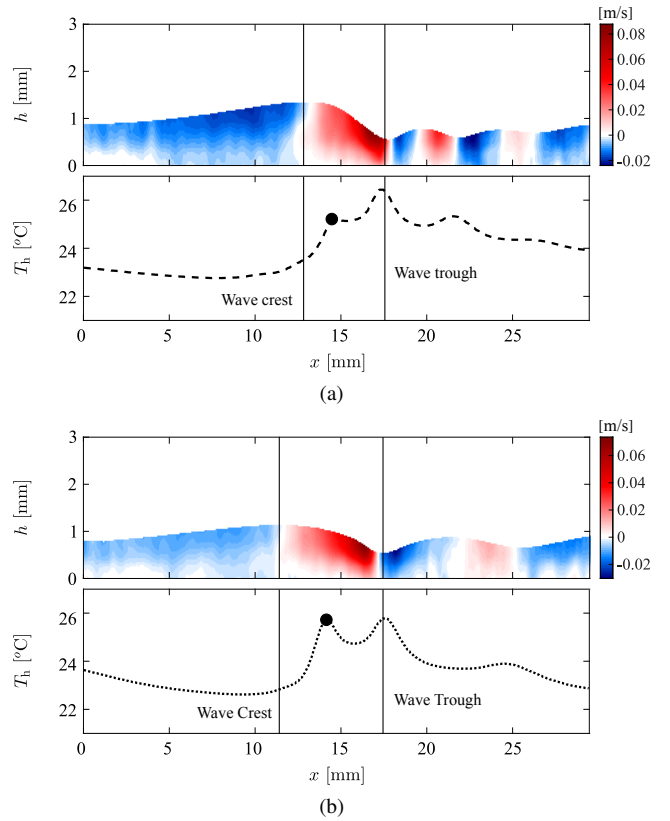The step-like increase in T_h when $f_w = 12$ Hz and $f_w =$

Figure 18: Phase-locked averaged cross-stream velocity, U_y, along the waves of flows with $Re = 28$, $\dot{q} = 2.5$ W cm^{-2} and: (a) $f_w = 12$ Hz and (b) 17 Hz, , presented alongside their interface temperature, T_h, data from Fig. 17. The black dots in the plots of T_h against x mark the locations of local overshoots in T_h, in the regions bounded by the wave crests and troughs.

17 Hz, in the region bounded by the solitary-wave crest and trough, is speculatively linked to the magnitude of the local cross-stream velocity components, and consequently, the amplitude of the local film-height fluctuations; specifically, the amplitude of the solitary waves which falls with increasing f_w, and the amplitude of the capillary waves preceding them, which increases instead. In Fig. 18, we present 2-D phase-locked averaged measurements of the cross-stream velocity component, U_y, from flows with $f_w = 12$ and 17 Hz, $Re = 28$ and $\dot{q} = 2.5$ W cm^{-2}, alongside their respective T_h data from Fig. 17. Based on this plot, we hypothesize that the positive (away from the wall) U_y underneath the solitary-wave crests are responsible for pushing hotter fluid from near the wall, towards the gas-liquid interface. This effect could underlie a significant heat transfer enhancement-mechanism by promoting mixing locally. Denner et al. [10] have shown, by conducting DNSs in isothermal falling-films in the drag-inertia regime, that the film-height fluctuations along the solitary waves induce large cross-stream velocity components locally. Furthermore, the variation of the cross-stream motion with the flow Re was shown to contribute to the saturation of the wave-crest height, following the onset of flow recirculation in a reference frame moving with the wave speed. The latter was accompanied by negative (downward) U_y under the wave crests and positive U_y behind the crests. Our 2-D U_y maps are in excellent qualitative agree-

ment with the data presented by Denner *et al.* [10] in the absence of flow recalculation; moreover $c > U_h$ for these cases, including the $f_w = 7$ Hz flow (Fig. 15(c)). Hence, the observed heat transfer enhancement does not rely on flow recirculation in that region.

4.5 Heat transfer measurements

In Refs. [12, 13], we presented space- and time-resolved film height and heat transfer data from water-ethanol film flows ($Pr = 5.4$) falling over a resistively heated, thin metal-foil, and commented on the physical mechanisms underlying the observed heat transfer gains compared to a steady film flow. In greater detail, we reported that the temperature distribution at the film free-surface was dominated by thermal rivulets which were attributed to Marangoni flows (i.e., flows driven by surface tension gradients which, in this case are induced by temperature gradients), and speculated that the source of the initial perturbation comprised localised temperature inhomogeneities at the interface. The ensuing surface tension gradients then drove a flow in the spanwise direction, which advected hot liquid from near the heated substrate and towards the gas-liquid interface. Further downstream, the long and thin thermal rivulets ("fingers") expanded spontaneously in the spanwise direction of the flow, and developed into regular rivulets that exhibited a quasi-sinusoidal modulation of the film-height. In addition to the rivulets, the coupling between the local and instantaneous film height and gas-liquid interface temperature featured prominently in these publications, and was shown to result in a strong coupling between the local and instantaneous film height and HTC at low and intermediate *Re* ($\approx 70 - 700$). At higher *Re*, the coupling between the two quantities was weaker potentially due to flow recirculation (in a reference frame moving with the wave speed) underneath the main wave humps. Still, the enhancement of the HTC at lower *Re*, which was primarily driven by the rivulets, was significant, exceeding the value that was predicted by the Nusselt description of the flow by up to a factor of 2.

The Nusselt description of the flow has been used in isothermal, as well as in heated film-flow investigations, in order to "benchmark" the results obtained in both experiments and simulations. Earlier, when assessing the validity of our combined optical technique, we showed how the film thickness and bulk and interface velocity of a Nusselt flow can be obtained by solving the Navier-Stokes equation after applying a number of simplifications (i.e., neglecting terms based on the assumptions of a gravity-driven, steady, fully-developed, 1-D flow). Similarly, the energy equation can be simplified in order to yield estimates of the gas-liquid interface and bulk-liquid temperatures, T_h and T_b, respectively:

$$T_h = T_w - \frac{2}{5}\frac{\dot{q}h}{\lambda_f} \tag{10}$$

and

$$T_b = T_w - \frac{5}{8}\frac{\dot{q}h}{\lambda_f} . \tag{11}$$

Aside from our earlier work, numerous researchers also reported on heat transfer enhancements in low-*Pr* falling-films (compared to flat films), which they attributed to the
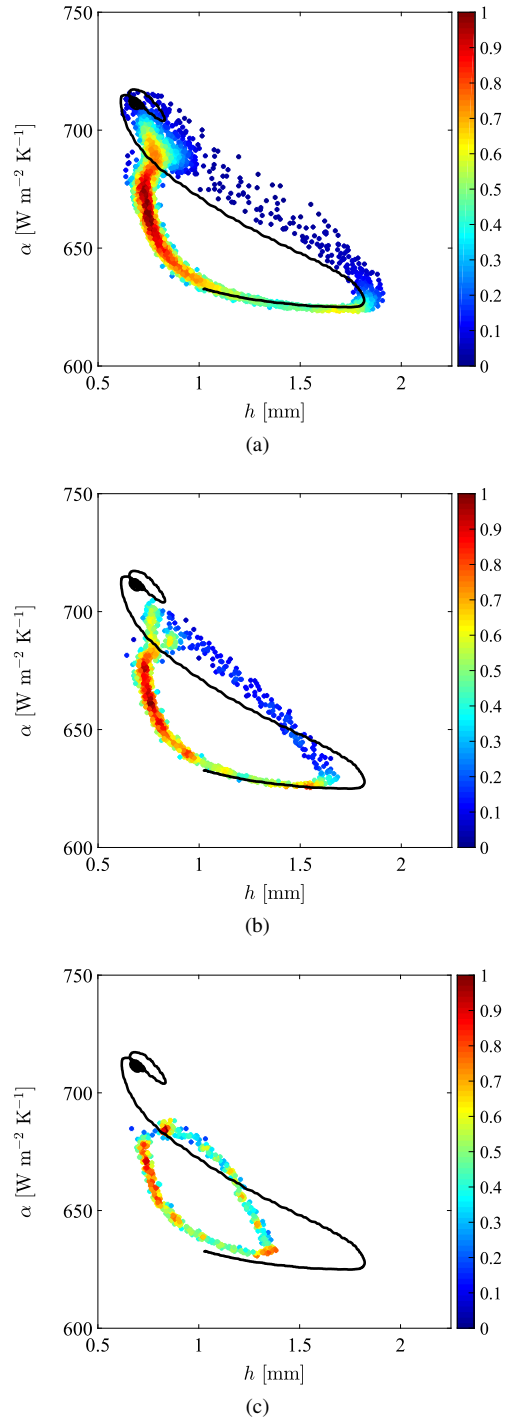

Figure 19: Local and instantaneous HTCs, plotted against their respective film heights, for a flow with $\dot{q} = 2.5\,\mathrm{W\,cm^{-2}}$, $f_w = 7$ Hz and $Re = 28$. Data were extracted and averaged from a flow region that extends over: (a) ≈ 1.4 mm, (b) ≈ 15 mm, and (c) ≈ 29 mm along the imaging domain. The colour scale represents the probability density calculated based on the bivariate distribution of the local and instantaneous HTC and film-height, while the solid black lines represent a phase-locked average measurement along the wave topology.

thinning of those films due to the waviness of the free-surface, and the formation and impact of thermal rivulets (see, for example, Refs. [13, 42, 45]). Instead, in high-*Pr* films, any gains are mainly convective in nature, and have

been traced back to flow recirculation underneath the wave crests (see, for example, Refs. [72, 73]).

The suppression of the development of thermal rivulets in the high-Pr, and relatively high-Re (given the liquid properties), films we investigate here presents us with a multitude of interesting avenues to explore. For example, we can decouple the effects of flow parameters such as the excitation frequency and flow Re, and heat transfer parameters such as the applied heat flux, from the heat transfer gains obtained due to thermal rivulets, and in that way establish a "baseline" for the heat transfer performance of unsteady film-flows. Furthermore, the impact of the time- and space-varying viscosity and its coupling to the flow field can be examined in detail, and largely in isolation from any Marangoni convection. The inception of thermal rivulets can also be examined by employment of the presented data, by systematically studying the observation of highly localized "hot-spots" on the film free-surface, which constitute the initial development stage of rivulet formation. These interfacial features can be observed in the IR images (see, for example, Fig. 5), arising spontaneously, mainly along the thinner and flatter regions of the film (more frequently so at low Re and f_w). As they are convected by the mean flow, their temperature increases until they are either consumed by the faster moving waves that catch up with them, or form elongated streaks. Lel *et al.* [45, 46] have, instead, observed quasi-regular, metastable thermal rivulets in high-Pr silicon-oil flows ($Pr = 57 - 177$); however, the liquid Ka (= $24 - 124$), inclination angle β (= $90\,°$) and flow Re (typically < 20) that were selected in these experiments are significantly different from our experiments, which could account for the different thermal features that we report here. It is also worth noting that in our experiments, depending on the flow Re, applied $\dot{q}$ and imposed f_w, the peak temperature of these spots can exceed that of the surrounding fluid by $\approx 5-20$ °C, resulting in significant heat transfer enhancements locally (in excess of 50%). The investigation of the formation and impact of these thermal features on the local and instantaneous HTC is beyond the scope of this study; however, a more systematic assessment will be presented in the future.

The upcoming analysis of the heat transfer performance of the examined $Pr = 77$ films, therefore, stretches past the investigation of such highly localized phenomena, and instead focuses on the link between large-amplitude fluctuations of the HTC and the interface height. We initiate this analysis by plotting local and instantaneous HTCs against their respective film heights for a flow with $\dot{q} = 2.5$ W cm^{-2}, $f_w = 7$ Hz, $Re = 28$, and a varying spatial extent of the film region we use in order to extract the relevant data, in Fig. 19. The colour scale represents the probability density calculated based on the bivariate distribution of the local and instantaneous HTC and film-height. Regarding the data presented in Fig. 19(a), we observe that h varies in the range $\approx 0.6 - 1.85$ mm, while a fluctuates in the range $\approx 625 - 720$ W m^{-2} K^{-1}. The coupling between the two quantities is strong, mainly along the thinner film regions (i.e., along the substrate film and capillary waves) where the heat extracted from the wall penetrates all the way to the free-surface. To the right of the main body of the displayed data (for $h > 1$ mm), there are two "zones" where the ma-

jority of the remaining data congregate. The lower-HTC data points emanate from the tails of the large-amplitude solitary waves, and the scarcer, higher-HTC data from the steep fronts of the solitary waves (i.e., between the crests and troughs).

Overlapping the data that were extracted from time-series of h and a are solid black lines that correspond to phase-locked average measurements of h and a along the waves (i.e., from behind the wave crest to the substrate film preceding the capillary ripples). This data, along with the data shown in Fig. 19(b) and (c), allow us to scrutinise the effect of the spatial extent of the film region that we use in order to extract local and instantaneous HTC and h values, on the observed coupling between the two quantities of interest. Specifically, the phase-locked average data carry over the spatial resolution of the PLIF/PTV measurements, while the spatial extent of the averaging region used to generate the time-series of h and a increases from ≈ 1.4 mm (Fig. 19(a)) to ≈ 15 mm (Fig. 19(b)) and then to ≈ 29 mm (see, Fig. 19(c)).

Referring to Fig. 19(a), we observe that whereas any phase-locked average data that emanate from behind the wave crest match the data from the time-series, any data that are extracted from film regions with large interface gradients (i.e., between the crest and trough) or small length scales (i.e., the capillary waves), do not fully overlap the time-series data points. Yet, the overall trend between a and h is largely conserved, as is the range that the film-height and HTC data span. Increasing the size of the averaging region to ≈ 15 mm results in is slightly narrower h and a ranges ($h \approx 0.7 - 1.7$ mm and $a \approx 625 - 700$ W m^{-2} K^{-1}). The same overall trend between the two quantities is still observed; however, the data points from the heavily-sloped regions between the solitary-wave crests and troughs are now encountered with higher probability. Finally, increasing the size of the averaging region to ≈ 29 mm results in a further reduction of the observed data ranges, and a more symmetric shape for the distribution of the data, with the axis of symmetry extending between the film-height and HTC extrema. It should be noted that the remarks we make here are somewhat dependent on the film topology, and thus the pulsation frequency, flow Re and liquid Ka. Increasing the wave frequency from $f_w = 7$ Hz to $f_w = 17$ Hz, for example, results in shorter wavelengths, the elimination of the substrate film, larger and longer capillary waves, and a weaker coupling between the HTC and h (Fig. 20).

In Fig. 20, we plot local and instantaneous HTCs (left column) and Nu (right column) against their respective film heights for flows with $\dot{q} = 2.5$ W cm^{-2}, $Re \approx 28$ and $f_w = 7$, 12 and 17 Hz. The black dotted lines represent the HTC/Nu that were calculated for flat-films over the same range of h. As the f_w is increased, the range of observed HTCs falls; a remark that can be linked to the reduction of the range of observed film-heights at higher f_w, as the amplitude of the solitary waves decreases and the spatial extent of the substrate film-region shrinks. For the same reason, the strong coupling between h and the HTC that we reported earlier for the $f_w = 7$ Hz flow becomes less pronounced; in fact, when $f_w = 17$ Hz, the measured HTCs congregate about the analytical solution and no distinct trend can be discerned. Interestingly, the data pairs that are encountered with the highest
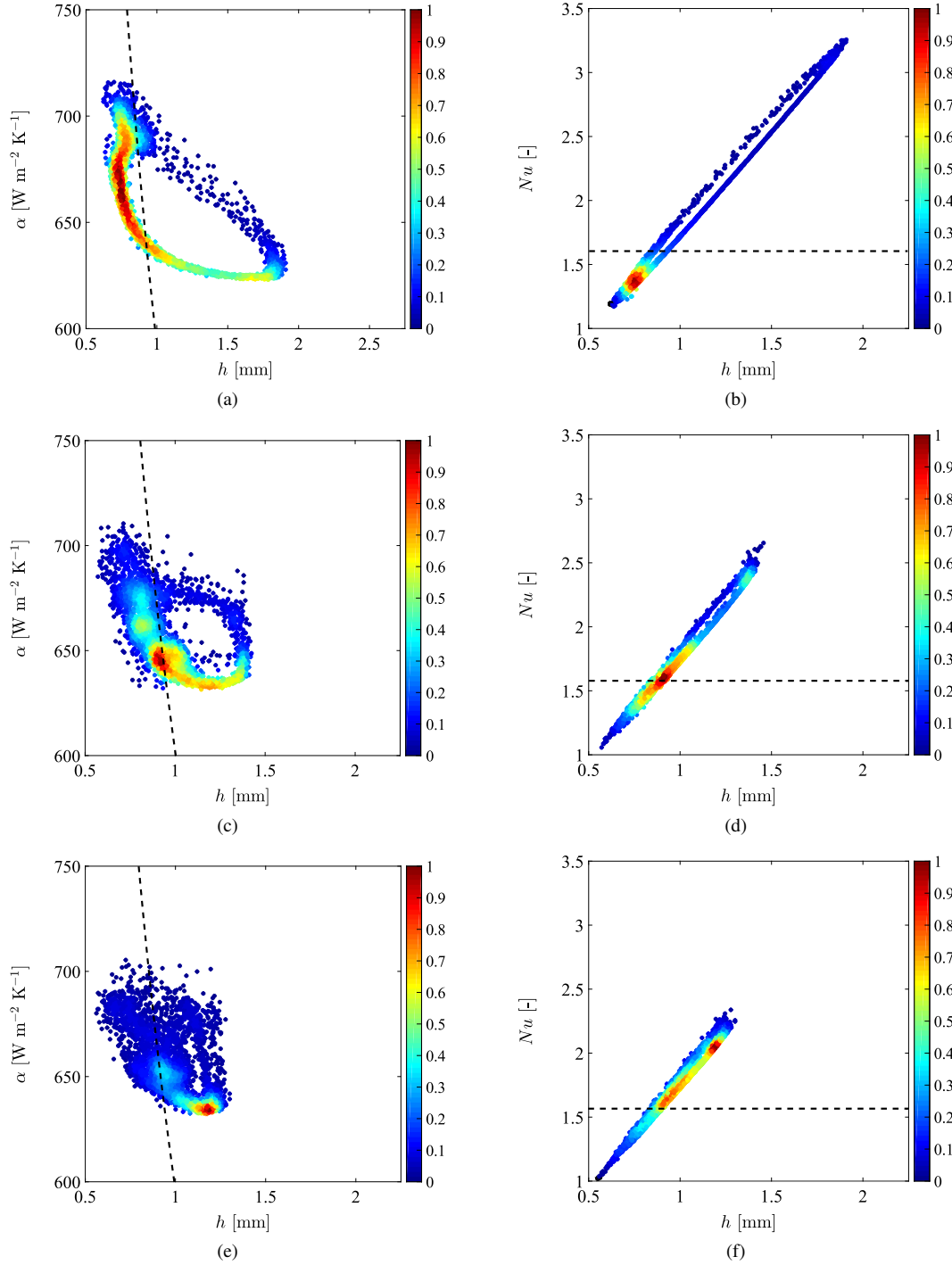
Figure 20: Local and instantaneous HTCs (left column) and Nu (right column), plotted against their respective film heights, for flows with $\dot{q} = 2.5\,\mathrm{W\,cm^{-2}}$, $Re \approx 28$ and: (a)-(b) $f_\mathrm{w} = 7$ Hz, (c)-(d) $f_\mathrm{w} = 12$ Hz, and (e)-(f) $f_\mathrm{w} = 17$ Hz. The colour scale represents the probability density calculated based on the bivariate distribution of the local and instantaneous HTC/Nu and film-height, while the dotted black lines represent the HTCs/Nu that were calculated for steady-film flows over the range of h that were observed in the experiments.

probability now lie to the right of the steady-flow curve. The observation of lower HTCs with higher probability as f_w is increased is most probably attributed to the differing evolution of the film topology along the streamwise direction of the flow, depending on the imposed f_w. In greater detail, we hypothesize that as the film heats up and its viscosity decreases, it accelerates and, given that the wave frequency is conserved, this leads to an increases in wavelength. The original topology (the one pertaining to an isothermal flow

of the same mean-flow rate and inlet temperature), which in the case of $f_\mathrm{w} = 17$ Hz comprises a single trough with no capillary ripples, cannot be sustained, and a capillary wave emerges ahead of the solitary-wave front (Fig. 12). This re-distribution of liquid also accounts for the non-monotonic increase of T_h with x along the IR imaging domain as well (see, Fig. 10 when $f_\mathrm{w} = 17$ Hz, in contrast to the $f_\mathrm{w} = 7$ Hz case), which provides evidence in support of our hypothesis.

Regarding the variation of the local and instantaneous

$Nu = ah/\lambda_\mathrm{f}$ with h (Fig. 20(b), (d) and (f)), we recover a trend that closely resembles a narrow ellipse. The coupling between the two quantities is very strong owing to the significantly larger variation of h compared to a; for example, for the $f_\mathrm{w} = 7$ Hz case, a increases by $\approx 16\%$ between the crest and trough, while h falls by nearly 300%. As anticipated, the range of observed Nu increases as the f_w is reduced, peaking at $Nu \approx 3.3$ for the $f_\mathrm{w} = 7$ Hz flow, and at $Nu \approx 2.7$ and $Nu \approx 2.4$ when $f_\mathrm{w} = 12$ and 17 Hz, respectively. Also plotted is the (constant) $Nu = 8/5$ that is obtained from the steady-flow analysis, based on the temperature difference across the liquid domain, $\Delta T = T_\mathrm{w} - T_\mathrm{h}$.

Compared to the low-Pr (= 5.4), $Re = 300$ data in Ref. [12], the trend that we observe here is notably different. In the case of the former, the Nu showed only small variations around $Nu = 4$ and over the range $h = 0.6 - 1.5$ mm; however, distinct peaks were identified near the wave crests and troughs. The peak corresponding to the crests may stem from the reduced coupling between a and h in the thicker film regions, while the peak at the troughs/substrate film may be attributed to gains induced by the thermal rivulets that were shown to spread over the film surface from very low values of $\dot{q}$ already, and with little dependence on the flow Re (see, Ref. [13]). Hence, those joint probability distributions may ensue from the overlap of two distinct effects; the one we report here when the film is at its thickest and any heating applied at the wall penetrates through the film only modestly, and a second in which the rise of hot fluid from near the wall to the film surface due to buoyancy and Marangoni convection when the film is thinner.

We now proceed to examine the coupling between the HTC and h as a function of the flow Re in Fig. 21, for flows $f_\mathrm{w} = 7$ Hz (i.e., the frequency that displays the strongest coupling). For the highest Re flow (= 66), h varies in the range $\approx 0.8 - 2.4$ mm and the HTC is near constant and equal to 685 W m^{-2} K^{-1}; it only deviates slightly from this value along the capillary waves and the wave fronts, which (like we showed earlier) display slightly higher HTCs than film regions with the same h from behind the wave crests. At the substrate film, which is encountered with the highest probability, the obtained HTCs match the theoretical prediction. Reducing the flow rate to $Re = 55$ results in a reduction in the range of observed film-heights, as the wave crest and trough heights fall. The heating at the wall now penetrates through the film and all the way to the free surface even at high values of h, and thus, the dependence of the HTC on the local and instantaneous film height becomes stronger. The variation of the HTC is still modest; however, the thicker film regions (solitary waves) display lower HTCs than before, while along the thinner film regions, such as the wave troughs, the peak HTC is still ≈ 685 W m^{-2} K^{-1}. Reducing the flow Re further (to $Re = 45$) accentuates the aforementioned effects, while when $Re = 35$, a strong coupling between the HTC and h can be clearly observed, particularly along the substrate film and capillary waves. In fact, the HTC displays almost the same sensitivity on h as suggested by theory along those regions of the flow. Another interesting observation relates to magnitude of the HTC in those regions, which is lower than analytical calculations suggest, and in contrast with the thicker film regions, where

the measured values exceed the analytical ones. Finally, for the $Re = 25$ film, the entire range of measured film heights ($h \approx 0.6 - 1.85$ mm) is coupled to the ΔT across the film.

The investigation of lower Re flows in our experiments was impeded by safety concerns, and specifically a potentially catastrophic failure of the glass substrate in the case of dewetting. Based on the collected data, however, we speculate that for lower Re, the film waviness would be further suppressed and the analytical approximation of the relationship between the local and instantaneous HTC and h would be observed within the ensuing narrow range of h. The emergence of hot-spots and thermal rivulets is, however, expected to boost convective heat transfer, resulting in higher HTCs and effectively translating the majority of the data upwards.

5 Conclusions

An optical technique that combines simultaneous planar laser-induced fluorescence (PLIF), particle tracking velocimetry (PTV) and infrared (IR) thermography was developed and applied towards the space- and time-resolved measurement of the film-height, 2-D velocity and 2-D free-surface temperature in liquid films flowing over an inclined ($\beta = 20$ °), resistively heated glass-substrate. Using this data and knowledge of the wall temperature along the fluid domain where optical measurements were conducted, local and instantaneous heat-transfer coefficients (HTCs) and Nusselt numbers, Nu, were also recovered. High-fidelity flow and heat transfer data were generated along the waves of film flows with $Re = 18 - 66$, $f_\mathrm{w} = 7$, 12 and 17 Hz, and $\dot{q} = 2.5$ W cm^{-2}, while complementary data were collected from equivalent isothermal flows (i.e., flows with the same Re and f_w, and $\dot{q} = 0$ W cm^{-2}) to help us benchmark the impact of heating on the hydrodynamics of the examined flows. To the best of our knowledge, this is the first instance whereby spatiotemporally resolved heat-transfer measurements are recovered simultaneously with spatiotemporally resolved flow measurements in falling liquid-films.

The employed water-glycerol solution comprises 55% glycerol by volume and is highly viscous ($\nu_\mathrm{f} = 9.2 \times 10^{-6}$ m^2 s^{-1} at 22 °C) and modestly (thermally) conductive ($\lambda_\mathrm{f} = 0.37$ Wm^{-1}K^{-1}), resulting in $Pr = 77$ and $Ka = 180$. These attributes suppress the development of thermal rivulets on the free-surface of the examined films, thus allowing us to decouple the effects of flow parameters such as the excitation frequency and flow Re from the heat transfer behaviour that would ensue otherwise. Another noteworthy attribute of the selected fluid is that its viscosity varies significantly along the streamwise direction of the flow. As the film extracts heat from the substrate it becomes progressively thinner and accelerates so that the mean flow rate is conserved.

Additional experiments were conducted to estimate the measurement uncertainty of the combined optical technique. In more detail, $Ka = 17 - 25$ flows were established in order to suppress the growth of large-amplitude waves, and film thickness data were extracted using PLIF and compared to analytical calculations based on the Nusselt solution to the Navier-Stokes equation. Based on this exercise, a measurement-uncertainty of 2% is quoted for any averaged (time- or phase-locked averaged) film height measurements.
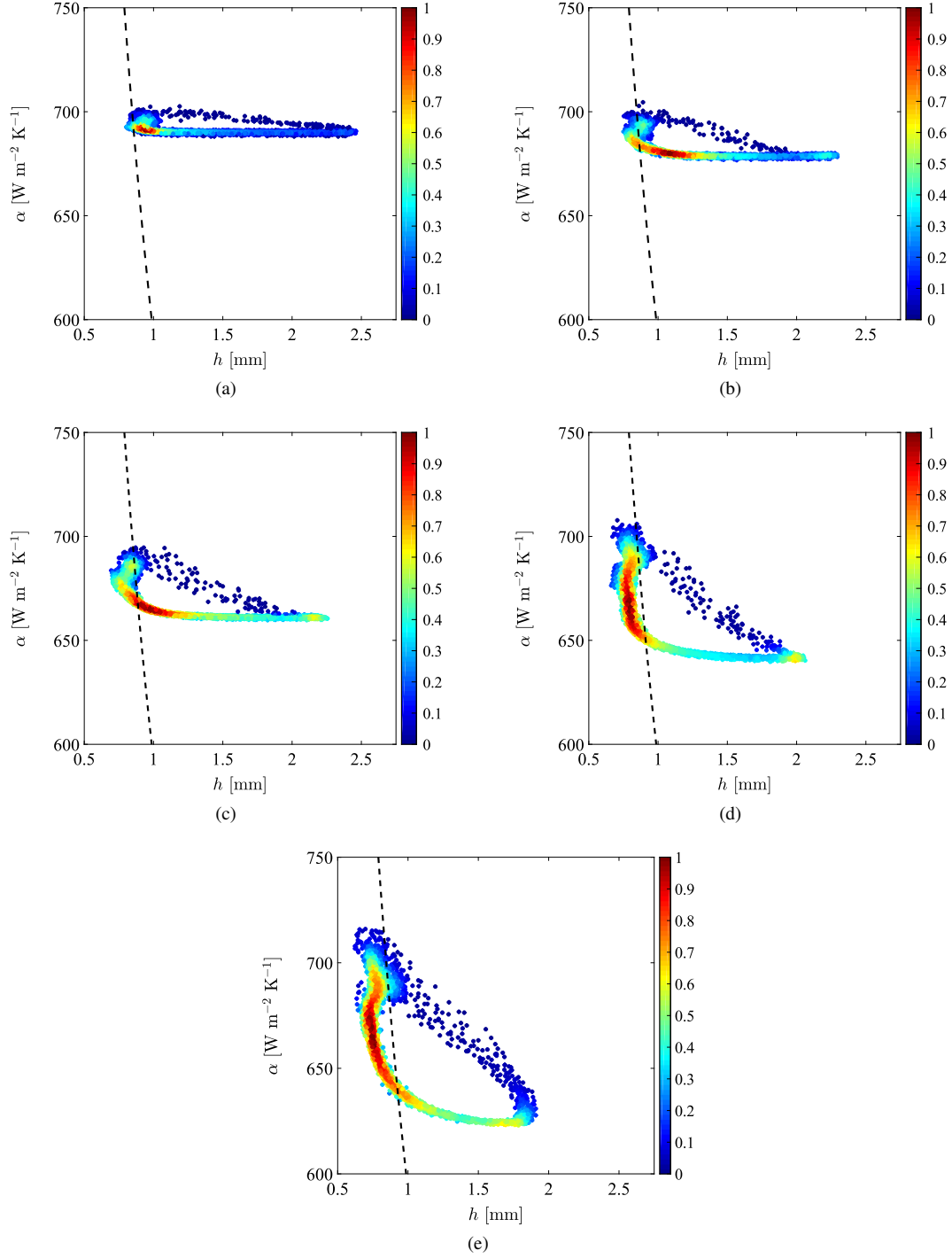
22

Figure 21: Local and instantaneous HTCs plotted against their respective film heights, for flows with $\dot{q} = 2.5\ \mathrm{W\,cm^{-2}}$, $f_\mathrm{w} = 7$ Hz and: (a) $Re = 65$, (b) $Re = 55$, (c) $Re = 45$, (d) $Re = 35$ and (e) $Re = 28$. The colour scale represents the probability density calculated based on the bivariate distribution of the local and instantaneous HTC and film-height, while the dotted black lines represent the HTCs that were calculated for steady-film flows over the range of h that were observed in the experiments.

Instantaneous and local film-height measurements, however, bear additional random errors and are thus assigned a mean relative uncertainty of $4 - 5\%$. The uncertainties associated with the measurement of the mean bulk and interface velocities from PTV were also estimated by pursuing comparisons to analytical calculations, and correspond to 3%. Finally, IR-based interface-temperature measurements were compared to thermocouple measurements in the range $20 - 40$ °C.

Based on the results of this study, the uncertainty of the interface-temperature measurement is < 1 °C.

Using the information we obtain by cross-correlating instantaneous film-height measurements about the waves, we generate phase-locked average film height, velocity field and interface-temperature measurements. The application of $\dot{q} = 2.5\ \mathrm{W\,cm^{-2}}$ at the solid wall results in a pronounced reduction of the mean film-heights (by 18%, on average)

compared to equivalent isothermal flows. Overall, the film waviness is higher for the heated films. The axial velocity profiles that were extracted along the waves are consistently "fuller" for the heated cases; yet, they are still parabolic excluding any wave-regions where the interface slopes are high, also in agreement with the isothermal cases. The bulk velocities are $\approx$ 18% higher, on average, for the heated films, thus compensating for the reduction in the mean-film heights. Our phase-locked averaged gas-liquid interface temperature measurements reveal that when f_w = 12 or 17 Hz, the temperature distributions along the waves vary non-monotonically with increasing distance from the flow inlet, possibly in response to variations in the interface topology which changes as the film heats up and the liquid viscosity decreases. At the PLIF/PTV imaging region, a "step-like" increase in T_h between the solitary-wave crests and troughs is observed at low Re (= 28). We speculate that this feature is linked to the locally strong cross-stream velocity components away from the wall, and could underlie a heat transfer enhancement-mechanism by promoting mixing locally.

The heat transfer characteristics of the examined films are scrutinised based on plots of the local and instantaneous HTC/Nu against the local and instantaneous film height. For the highest Re flows (= 66), the HTC is near constant; reducing the Re triggers an overall reduction in the range of observed film-heights, allowing the heating at the wall to penetrate to the free surface. Below Re = 35, a strong coupling between the HTC and h is reported, especially along the substrate film and capillary waves. In fact, the HTC displays almost the same sensitivity on h as suggested by the Nusselt description of the flow. With increasing f_w, the range of observed HTCs falls due to the reduction in the range of observed film-heights. For the same reason, the coupling between h and the HTC becomes less pronounced, and the film height/HTC pairs that are encountered with the highest probability migrate the right of the steady-flow curve. We speculate that the observation of lower-HTC data points with higher probability at higher f_w is linked to the evolution of the film topology along the streamwise direction of the flow. Regarding the variation of the local and instantaneous Nu, we recover a trend that closely resembles a narrow ellipse. A pronounced coupling between the two quantities is reported, and is attributed to the significantly larger variation of h compared to the HTC. The range of observed Nu increases as the f_w is reduced.

In the future, we aim to complement our experiments with results from direct numerical simulations (DNSs) based on the methodologies presented in Denner *et al.* [69–71], from which the film height as well as the full temperature, viscosity and velocity fields in the liquid domain upstream of the PLIF/PTV measurement location will be computed, thus allowing greater insight into the complex flow behaviour underlying the examined flows. Of particular interest is the study of the highly localized "hot-spots" that we observe systematically on the film free-surface, and the understanding of the impact of these events on the variation of the local and instantaneous HTC and Nu and their time averages.

Acknowledgments

References

[1] S.W. Joo, S.H. Davis, and S.G. Bankoff. A mechanism for rivulet formation in heated falling films. *J. Fluid Mech.*, 321:279–298, 1996.

[2] B. Scheid, S. Kalliadasis, C. Ruyer-Quil, and P. Colinet. Interaction of three-dimensional hydrodynamic and thermocapillary instabilities in film flows. *Phys. Rev. E*, 78:066311–1–16, 2008.

[3] A.V. Cherdantsev, D.B. Hann, and B.J. Azzopardi. Study of gas-sheared liquid film in horizontal rectangular duct using high-speed LIF technique: Three-dimensional wavy structure and its relation to liquid entrainment. *Int. J. Multiphase Flow*, 67:52–64, 2014.

[4] G. Karimi and M. Kawaji. Flow characteristics and circulatory motion in wavy falling films with and without counter-current gas flow. *Int. J. Multiphase Flow*, 25 (6–7):1305–1319, .

[5] B. Scheid, N. Kofman, and W. Rohlfs. Critical inclination for absolute/convective instability transition in inverted falling films. *Phys. Fluids*, 28:044107–1–15, 2016.

[6] A. Charogiannis and C.N. Markides. Application of planar laser-induced fluorescence for the investigation of interfacial waves and rivulet structures in liquid-films flowing down inverted substrates. *Interfacial Phenom. Heat Transf.*, 4:235–252, 2016.

[7] A. Charogiannis, J.S. An, and Markides. C.N. A simultaneous planar laser-induced fluorescence, particle image velocimetry and particle tracking velocimetry technique for the investigation of thin liquid-film flows. *Exp. Therm. Fluid Sci.*, 68:516–536, 2015.

[8] A. Charogiannis, F. Denner, B.G.M. van Wachem, S. Kalliadasis, and C.N. Markides. Detailed hydrodynamic characterization of harmonically excited falling-film flows: A combined experimental and computational study. *Phys. Rev. Fluids*, 2:014002–1–37, 2016.

[9] A. Charogiannis, F. Denner, B.G.M. van Wachem, S. Kalliadasis, and C.N. Markides. Statistical characteristics of falling-film flows: A synergistic approach at the crossroads of direct numerical simulations and experiments. *Phys. Rev. Fluids*, 2:124002–1–28, 2017.

[10] F. Denner, A. Charogiannis, M. Pradas, C.N. Markides, B.G.M. van Wachem, and S. Kalliadasis. Solitary waves on falling liquid films in the inertia-dominated regime. *J. Fluid Mech.*, 837:491–519, 2018.

[11] F. Denner, M. Pradas, A. Charogiannis, C.N. Markides, B.G.M. van Wachem, and S. Kalliadasis. Self-similarity of solitary waves on inertia-dominated falling liquid films. *Phys Rev E.*, 93:033121–1–14, 2016.

[12] R. Mathie, H. Nakamura, and C.N Markides. Heat transfer augmentation in unsteady conjugate thermal systems – Part II: Applications. *Int. J. Heat Mass Transfer*, 56(1–2):819–833, 2013.

[13] C.N. Markides, R. Mathie, and A. Charogiannis. An experimental characterization of spatiotemporally resolved heat transfer in thin liquid-film flows falling over an inclined heated foil. *Int. J. Heat Mass Transfer*, 93:872–888, 2016.

[14] A. Charogiannis, F. Denner, B.G.M. van Wachem, S. Kalliadasis, B. Scheid, and C.N. Markides. Experimental study of liquid films flowing down and under an inclined planar substrate. *Phys. Rev. Fluids*, *Submitted, Under Review*, 2018.

[15] S. Alekseenko, A. Cherdantsev, M. Cherdantsev, S. Isaenkov, S. Kharlamov, and D. Markovich. Application of a high-speed laser-induced fluorescence technique for studying the three-dimensional structure of annular gas-liquid flow. *Exp. Fluids*, 53:77–89, 2012.

[16] I. Zadrazil, O.K. Matar, and C.N. Markides. An experimental characterization of downwards gas-liquid annular flow by laser-induced fluorescence: Flow regimes and film statistics. *Int. J. Multiphase Flow*, 60:87–102, 2014.

[17] A. Cherdantsev, D.B. Hann, B.N. Hewakandamby, and B.J. Azzopardi. Study of the impacts of droplets deposited from the gas core onto a gas-sheared liquid film. *Int. J. Multiphase Flow*, 88:69–86, 2017.

[18] G.F. Hewitt, S. Jayanti, and C.B. Hope. Structure of thin liquid films in gas-liquid horizontal flow. *Int. J. Multiph. Flow*, 16(6):951–957, 1990.

[19] R.G. Morgan, C.N. Markides, C.P. Hale, and G.F. Hewitt. Horizontal liquidliquid flow characteristics at low superficial velocities using laser-induced fluorescence. *Int. J. Multiphase Flow*, 43:101–117, 2012.

[20] R.G. Morgan, C.N. Markides, I. Zadrazil, and Hewitt. Characteristics of horizontal liquidliquid flows in a circular pipe using simultaneous high-speed laser-induced fluorescence and particle velocimetry. *Int. J. Multiphase Flow*, 49:99–118, 2013.

[21] R.G. Morgan, R. Ibarra, I. Zadrazil, O.K. Matar, G.F. Hewitt, and C.N. Markides. On the role of buoyancy-driven instabilities in horizontal liquid-liquid flow. *Int. J. Multiphase Flow*, 89:123–135, 2017.

[22] V. Voulgaropoulos and P. Angeli. Optical measurements in evolving dispersed pipe flows. *Exp. Fluids*, 58(170):1–15, 2017.

[23] A. Schagen, M. Modigell, G. Dietze, and R. Kneer. Simultaneous measurement of local film thickness and temperature distribution in wavy liquid films using a luminescence technique. *Int. J. Heat Mass Transfer*, 49(25–26):5049–5061, 2006.

[24] I. Zadrazil and C.N. Markides. An experimental characterization of liquid films in downwards co-current gas-liquid annular flow by particle image and tracking velocimetry. *Int. J. Multiphase Flow*, 67:42–53, 2014.

[25] A.C. Ashwood, S.J. Vanden Hogen, M.A. Rodarte, C.R. Kopplin, D.J. Rodrguez, E.T. Hurlburt, and T.A. Shedd. A multiphase, micro-scale PIV measurement technique for liquid film velocity measurements in annular two-phase flow. *Int. J. Multiph. Flow*, 68:27–39, 2015.

[26] D. Schubring, A.C. Ashwood, T.A. Shedd, and E.T. Hurlburt. Planar laser-induced fluorescence (PLIF) measurements of liquid film thickness in annular flow. Part I: Methods and data. *Int. J. Multiph. Flow*, 36(10): 815–824, 2010.

[27] P.S.C. Farias, F.J.W.A. Martins, L.E.B. Sampaio, R. Serfaty, and L.F.A. Azevedo. Liquid film characterization in horizontal, annular, two-phase, gas-liquid flow using time-resolved laser-induced fluorescence. *Exp. Fluids*, 52(3):633–645, 2012.

[28] J Coppeta and C. Rogers. Dual emission laser induced fluorescence for direct planar scalar behavior measurements. *Exp. Fluids*, 25(1):1–15, 1998.

[29] J.A. Sutton, B. Fisher, and J.W. Fleming. A laser-induced fluorescence measurement for aqueous fluid flows with improved temperature sensitivity. *Exp. Fluids*, 45(5):869–881, 2008.

[30] P. Chamarthy, S. V. Garimella, and S. T. Wereley. Measurement of the temperature non-uniformity in a microchannel heat sink using microscale laser-induced fluorescence. *Int. J. Heat Mass Tran.*, 53.

[31] D. Ross, M. Gaitan, and L E. Locascio. Temperature measurement in microfluidic systems using a temperature-dependent fluorescent dye. *Analytical Chemistry*, 73(17):4117–4123, 2001.

[32] A. Schagen and M. Modigell. Local film thickness and temperature distribution measurement in wavy liquid films with a laser-induced luminescence technique. *Exp. Fluids*, 43(2–3):209–221, 2007.

[33] P. Adomeit and U. Renz. Hydrodynamics of three-dimensional waves in laminar falling films. *Int. J. Multiph. Flow*, 26(7):1183–1208, 2000.

[34] S.V. Alekseenko, V. Antipin, A. Cherdantsev, S. Kharlamov, and D. Markovich. Two-wave structure of liquid film and wave interrelation in annular gas-liquid flow with and without entrainment. *Phys. Fluids*, 21 (6):061701–1–4, 2009.

25

[35] S.M. Kharlamov, V.V. Guzanov, A.V. Bobylev, S.V. Alekseenko, and D.M. Markovich. The transition from two-dimensional to three-dimensional waves in falling liquid films: Wave patterns and transverse redistribution of local flow rates. *Phys. Fluids*, 27(11):114106–1–25, 2015.

[36] A.V. Cherdantsev, J.S. An, A. Charogiannis, and C.N. Markides. Cross-validation of PLIF and BBLIF towards the detailed study of gas-sheared liquid films in downward annular flows. *In Proceedings of the 19ᵗʰ International Symposium on the Application of Laser and Imaging Techniques to Fluid Mechanics*, Lisbon, Portugal, July 16 – 19, 2018.

[37] E.A. Chinnov and O.A. Kabov. Marangoni effect on wave structure in liquid films. *Microgravity Sci. Technol.*, 19(3–4):18–22, 2007.

[38] E.A. Chinnov and E.N. Shatskii. Effect of thermocapillary perturbations on the wave motion in heated falling liquid film. *Tech. Phys. Lett.*, 36(1):53–56, 2010.

[39] E.A. Chinnov, E.N. Shatskii, and O.A. Kabov. Evolution of the temperature field at the three-dimensional wave front in a heated liquid film. *High Temp.*, 50(1): 98–105, 2012.

[40] E.A. Chinnov and S.S. Abdurakipov. Thermal entry length in falling liquid films at high Reynolds numbers. *Int. J. Heat Mass Transfer*, 56(1–2):775–786, 2013.

[41] E.A. Chinnov. Wave – Thermocapillary effects in heated liquid films at high Reynolds numbers. *Int. J. Heat Mass Transfer*, 71:106–116, 2014.

[42] O.A. Kabov, B. Scheid, I.A. Sharina, and J.-C. Legros. Heat transfer and rivulet structures formation in a falling thin liquid film locally heated. *Int. J. Therm. Sci.*, 41(7):664–672, 2002.

[43] A. Charogiannis, I. Zadrazil, and C.N. Markides. Thermographic particle velocimetry (TPV) for simultaneous interfacial temperature and velocity measurements. *Int. J. Heat Mass Transfer*, 97:589–595, 2016.

[44] M. Rietz, W. Rohlfs, R. Kneer, and B. Scheid. Experimental investigation of thermal structures in regular three-dimensional falling films. *Eur. Phys. J. Special Topics*, 224(2):355–368, 2015.

[45] V.V. Lel, A. Kellerman, G. Dietze, R. Kneer, and A.N. Pavlenko. Investigations of the Marangoni effect on the regular structures in heated wavy liquid films. *Exp. Fluids*, 44(2):341–354, 2008.

[46] V. Lel, H. Stadler, A. Pavlenko, and R. Kneer. Evolution of metastable quasi-regular structures in heated wavy liquid films. *Heat Mass Transfer*, 43(11):1121–1132, 2007.

[47] F. Zhang, X. Zhao, J. Geng, Y.-T. Wu, and Z. Zhang. A new insight into Marangoni effect in non-isothermal falling liquid films. *Exp. Therm Fluid Sci.*, 31(4):361–365, 2007.

[48] F. Zhang, J. Peng, J. Geng, Z.-X. Wang, and Z.-B. Zhang. Thermal imaging study on the surface wave of heated falling liquid films. *Exp. Therm Fluid Sci.*, 33(3):424–430, 2009.

[49] F. Chen, H. Li, and H. Hu. Molecular tagging techniques and their applications to the study of complex thermal flow phenomena. *Acta. Mech. Sin.*, 31(4):425–445, 2015.

[50] K. Moran, J. Inumaru, and M. Kawaji. Instantaneous hydrodynamics of a laminar wavy liquid film. *Int. J. Multiph. Flow*, 28(5):731–755, 2002.

[51] G. Karimi and M. Kawaji. An experimental study of freely falling films in a vertical tube. *Chem. Eng. Sci.*, 53(20):3501–3512, 1998.

[52] G. Karimi and M. Kawaji. Flow characteristics and circulatory motion in wavy falling films with and without counter-current gas flow. *Int. J. Multiph. Flow*, 25 (6–7):1305–1319, .

[53] G.F. Dietze, F. A. Leefken, and R. Kneer. Investigation of the backflow phenomenon in falling liquid films. *J. Fluid Mech.*, 595:435–459, 2008.

[54] S.V. Alekseenko, V.E. Nakoryakov, and B.G. Pokusaev. Wave formation on a vertical falling liquid film. *AIChE J.*, 31(9):1446–1460, 1985.

[55] S.V. Alekseenko, V.A. Antipin, A.V. Bobylev, and D.M. Markovich. Application of PIV to velocity measurements in a liquid film flowing down an inclined cylinder. *Exp. Fluids*, 43(2–3):197–207, 2007.

[56] W. Rohlfs, P. Pischke, and B. Scheid. Hydrodynamic waves in films flowing under an inclined plane. *Phys. Rev. Fluids*, 2:044003–1–23, 2017.

[57] G.F. Dietze, F. Al-Sibai, and R. Kneer. Experimental study of flow separation in laminar falling liquid films. *J. Fluid Mech.*, 637:73–104, 2009.

[58] D. Reck and N. Aksel. Recirculation areas underneath solitary waves on gravity-driven film flows. *Phys. Fluids*, 27(11):112107–1–10, 2015.

[59] D. Schubring, R.E. Foster, D.J. Rodriguez, and T.A. Shedd. Two-zone analysis of wavy two-phase flow using micro-particle image velocimetry (micro-PIV). *Meas. Sci. Technol.*, 20(6):1–11, 2009.

[60] S. Kalliadasis, C. Ruyer-Quil, B. Scheid, and M.G. Velarde. *Falling Liquid Films*, volume 176 of *Applied Mathematical Sciences*. Springer Verlag, Berlin, 2012.

[61] A. Charogiannis, F. Denner, B.G.M. van Wachem, Kalliadasis, and C.N. Markides. A combined experimental and computational study of the heat transfer characteristics of falling liquid-films. *In Proceedings of the 3ʳᵈ Thermal and Fluids Engineering Conference (TFEC)*, Fort Lauderdale, FL, USA, March 4 – 7, 2018.

[62] M.Q. Brewster. *Thermal Radiative Transfer and Properties*. Wiley-Interscience, 1992.

[63] W. Nusselt. Die oberflachenkondensation des wasser-dampfes. *VDI Zeit.*, 60:541, 1916.

[64] C.J. Kähler, U. Scholtz, and J. Ortmanns. Wall-shear-stress and near-wall turbulence measurements up to single pixel resolution by means of long-distance micro-PIV. *Exp. Fluids*, 41(2):327–341, 2006.

[65] N.-S. Cheng. Formula for the viscosity of a glycerol-water mixture. *Ind. Eng. Chem. Res*, 47(9):3285–3288, 2015.

[66] R.B. Leron, A.N. Soriano, and M-H. Li. Densities and refractive indices of the deep eutectic solvents (choline chloride + ethylene glycol or glycerol) and their aqueous mixtures at the temperature ranging from 298.15 to 333.15 K. *J. Taiwan Inst. Chem. Engrs*, 43(4):551–557, 2012.

[67] E.I.P. Drosos, S.V. Paras, and A.J. Karabelas. Characteristics of developing free falling films at intermediate Reynolds and high Kapitza numbers. *Int. J. Multiph. Flow*, 30(7–8):853–876, 2004.

[68] T.D. Karapantsios, S.V. Paras, and A.J. Karabelas. Statistical characteristics of free falling films at high reynolds numbers. *Int. J. Multiph. Flow*, 15(1):1–21, 1989.

[69] F. Denner and B.G.M. van Wachem. Fully-coupled balanced-force vof framework for arbitrary meshes with least-squares curvature evaluation from volume fractions. *Numer. Heat Trans. B*, 65(3):218–255, 2014.

[70] F. Denner and B.G.M. van Wachem. Compressive VOF method with skewness correction to capture sharp interfaces on arbitrary meshes. *J. Comput. Phys*, 279:127–144, 2014.

[71] F. Denner and B.G.M. van Wachem. Numerical time-step restrictions as a result of capillary waves. *J. Comput. Phys*, 279:24–40, 2015.

[72] A. Miyara. Numerical analysis on flow dynamics and heat transfer of falling liquid films with interfacial waves. *Heat Mass Transfer*, 35(4):298–306, 1999.

[73] F. Al-Sibai, A. Leefken, and U. Renz. Local and instantaneous distribution of heat transfer rates through wavy films. *Int. J. Therm. Sci.*, 41(7):658–663, 2002.